MODELING OF REVERSE WATER-GAS SHIFT REACTION IN MEMBRANE INTEGRATED MICROREACTORS

by

Mert Can İnce

B.S., Chemical Engineering, Istanbul Technical University, 2020

Submitted to the Institute for Graduate Studies in
Science and Engineering in partial fulfillment of
the requirements for the degree of
Master of Science

Graduate Program in Chemical Engineering

Boğaziçi University

2023

ACKNOWLEDGEMENTS

I would like to express my biggest gratitude to Prof. Dr. Ahmet Kerim Avcı as my mentor and supervisor. His in-depth knowledge, methods and vision have led me to expand my knowledge and point of views in academic life. I can sincerely say that I consider myself as privileged for being chosen to be supervised by him especially in the beginning of my academic career. His guidance and vision paved the way more than letting me accomplishing my research.

I also would like to thank Assoc. Prof. A. Kerem Uğuz and Prof. Deniz Üner for devoting their valuable time to read and evaluate my research.

Special thanks to Hayrettin Hasan Köybaşı for his friendship and collaboration during my studies. I would like to thank every member of KB 404 for their valuable friendship, sincerity, “tea breaks” and academic help; Necdet Semih Altınsoy, Mert Özden, Özge Selçuk, Emre Küçük and Orhun Harmancılar. We created great memories together and many thanks for the warm atmosphere in our lab.

I would like to thank my friends from undergradute; Ece Meteris, Sibel Şentürk, Pınar Kurtuluş and Bilge Su Subaşı for their support during my studies, also contributing and sharing my joyfull life.

I would like to thank my brother Can Yakın from deepest of my heart. I would like to say that you are very special and important to me. I am lucky to have a buddy like you in my life. We had great memories together since first grade in primary school and I hope we will add so much more on.

I would like to express my love for my family. Firstly, I would like to thank my parents Orhan İnce and Bahar İnce for their infinite love and support. They are more than parents to me, they are also my teachers, advisors and guides in life. I am so lucky to have them as my father and mother, no matter how hard I try It wouldn't be enough to repay their effort. Secondly, I would like to thank my beloved sister Zeynep İnce. She supported me more than she thinked, sometimes she became a big sister to me. I love you more than world and you will always be my little princess. Also, I would like to commemorate and thank to my grandparents; Münevver İnce, Gülseren Kasapgil, Hamdi İnce and Hacı Mehmet Kasapgil. They became a role model to me, and many many thanks for this great family.

Finally, I would like to acknowledge TUBITAK for granting me a M.Sc. degree scholarship. Financial support is provided by TUBITAK project no: 120M412.

ABSTRACT

MODELING OF REVERSE WATER-GAS SHIFT REACTION IN MEMBRANE INTEGRATED MICROREACTORS

Synthesis gas (syngas) production by reverse water-gas shift (RWGS) reaction is modeled in a membrane integrated microchannel reactor. Process intensification is performed by *in-situ* steam separation *via* a hydrophilic α-Al_2O_3 supported sodalite membrane (SOD), which allows selective transport of H_2O and H_2 molecules. CuO/ZnO/Al_2O_3 (CZA) catalyst is considered as a layer that is washcoated to the inner walls of the rectangular shaped reaction channels of the microreactor. Pure H_2, readily available as a reactant, is used as the sweep gas in the permeate channel. Two dimensional, steady–state, isothermal operation of the intensified reactor is quantified by the momentum and mass conservations in the entire flow domain, membrane material transfer and catalytic reaction. The reactor is operated at 523 K, 5-15 bar and inlet molar H_2:CO_2 ratio = 2-4 and the effects of inlet velocities of the reactive mixture (H_2+CO_2) and sweep gas (H_2), reactor pressure, molar inlet H_2:CO_2 ratio and flow partitioning on per cent CO_2 conversion, amount of CO_2 converted and the synthesis gas composition are studied. Membrane assisted efflux of H_2O from/influx of H_2 into the reaction channel significantly improves the performance. A non-isothermal study is conducted to demonstrate that the microchannel system has the characteristics of near-isothermal conditions. The effect of flow direction on the reactor operation is found to be negligible. Sweep gas inlet velocity affected the performance metrics significantly. Integration of steam selective membrane and increasing sweep velocity to six times of the reaction channel inlet velocity showed an increase in CO_2 conversion from 16.1% to 51.6%. Sizing studies point out that 3.6 m^3 multichannel reactor can process H_2 input from a 1 MW commercial electrolyzer. The current reactor is also benchmarked with an equivalently operated packed-bed membrane reactor.

ÖZET

TERS SU-GAZI DEĞİŞİMİ REAKSİYONUNUN MEMBRAN ENTEGRE EDİLMİŞ MİKROREAKTÖRLERDE MODELLENMESİ

Membranlı mikrokanal reaktördeki RWGS reaksiyonu modellenmiştir. Proses yoğunlaştırma, H_2O ve H_2 moleküllerinin seçici taşımına izin veren hidrofilik α-Al_2O_3 destekli sodalite (SOD) membran kullanılarak yerinde buhar ayırma ile gerçekleştirilmiştir. CuO/ZnO/Al_2O_3 (CZA) katalizör tabakası, mikroreaktörün dikdörtgen şeklindeki reaksiyon kanallarının iç duvarları boyunca kaplanmıştır. Reaktan olarak da halihazırda bulunan saf H_2, süpürme kanalında süpürme gazı olarak kullanılmıştır. Yoğunlaştırılmış reaktörün iki boyutlu, yatışkın hal ve izotermal çalışma koşullarında, tüm akış alanı, membran kütle transferi ve katalitik reaksiyonu momentum ve kütle korunumları ile hesaplanmıştır. Reaktör, 523 K, 5-15 bar ve H_2:CO_2 giriş molar oranı = 2-4 olacak şekilde çalıştırılmıştır. Reaktif karışımın (H_2+CO_2) ve süpürme gazının (H_2) giriş hızlarının, reaktör basıncının, H_2:CO_2 molar giriş oranının ve akış yönünün yüzde CO_2 dönüşümü, dönüştürülen CO_2 miktarı ve sentez gazı bileşimi üzerindeki etkileri incelenmiştir. H_2O'nun reaksiyon kanalından dışarı/ H_2'nin süpürme kanalından içeri membran destekli akışı reaktör performansını önemli ölçüde arttırmıştır. Mikrokanal sistemin izotermale yakın koşulların karakteristik özelliklerine sahip olduğunu göstermek için izotermal olmayan koşullarda çalışma yürütülmüştür. Akış yönünün reaktörün çalışması üzerindeki etkisinin ihmal edilebilir olduğu saptanmıştır. Süpürme gazı giriş hızının, performans ölçütlerini önemli şekilde etkilediği gözlenmiştir. Buhar seçici membran entegrasyonu ile süpürme hızının reaksiyon kanalı giriş hızının altı katına çıkarılması, CO_2 dönüşümünü %16,1'den %51,6'ya çıkarmıştır. Boyutlandırma çalışmaları, 3,6 m^3'lük çok kanallı reaktörün, 1 MW'lık ticari bir elektrolizörden gelen H_2 girdisini işleyebileceğini göstermektedir. Ayrıca, mevcut reaktör birebir aynı şartlarda çalışan dolgu yataklı bir membran reaktör ile kıyaslanmıştır.

TABLE OF CONTENTS

ACKNOWLEDGEMENTS iii
ABSTRACT v
ÖZET vi
LIST OF FIGURES ix
LIST OF TABLES xii
LIST OF SYMBOLS xiv
LIST OF ACRONYMS/ABBREVIATIONS xvi
1. INTRODUCTION 1
2. LITERATURE SURVEY 5
2.1. Reverse Water-Gas Shift Reaction 5
2.1.1. Thermodynamic Analysis 5
2.1.2. Catalysts and Reaction Kinetics 6
2.1.2.1. Precious Metal Based Catalysts 6
2.1.2.2. Non-Noble Metal Based Catalysts 8
2.1.2.3. Metal Carbide Catalysts 15
2.1.2.4. Reaction Kinetics 16
2.2. Intensification of the Reverse Water-Gas Shift Reaction 19
2.2.1. Sorption Enhanced Reactors 19
2.2.2. Membrane Reactors 21
2.2.3. Microchannel Reactors 23
2.2.4. Structured Membrane Reactors 25
2.3. Steam Selective Membranes 26
3. MATHEMATICAL MODELING 28
3.1. Description of the Multifunctional Reactor 28
3.2. Reaction Network and the Kinetic Model 32
3.3. Membrane Model 34
3.4. Solution Methodology and Associated Equations 36
4. RESULTS AND DISCUSSION 39

4.1. Model Verification 39
4.2. Validation of Isothermal Conditions 40
4.3. Effects of Reactor Pressure, Reaction and Permeate Channel Inlet Velocities on CO_2 Conversion and the Amount of CO_2 Converted 41
4.4. Effects of Reactor Pressure, Reaction and Permeate Channel Inlet Velocities and H_2:CO_2 Ratio on Syngas Composition 47
4.5. Comparison of the Microchannel and Packed-Bed Membrane Reactors 50
4.6. Effect of Molar Inlet H_2:CO_2 Ratio on CO_2 conversion 51
4.7. Impact of Permeate Channel Flow Configuration 52
5. CONCLUSION 54
5.1. Conclusions 54
5.2. Recommendations 55
REFERENCES 56
APPENDIX A: PACKED-BED MEMBRANE REACTOR MODEL EQUATIONS 64

LIST OF FIGURES

Figure 1.1. World total energy supply by source between 1971 and 2019 [4]. 1

Figure 3.1. Schematic illustration of the multichannel reactor (left) and the unit cell (right). 28

Figure 3.2. Illustration of membrane model. 35

Figure 3.3. Representation of microchannel reactor boundary conditions. 37

Figure 4.1. Comparison between the experimental data and the data predicted from the model (T = 523 K, P = 1 bar, H_2:CO_2 = 6). 39

Figure 4.2. Temperature change along the reactor in co and counter-current flow configurations (T = 523 K, P = 5 bar, H_2:CO_2 = 3). 41

Figure 4.3. Effect of reaction and permeate channel inlet velocities on CO_2 conversion at 5 bar (T = 523 K, H_2:CO_2 = 3, flow direction in membrane–integrated cases: co–current). 42

Figure 4.4. Effect of reaction and permeate channel inlet velocities on converted CO_2 amount at 5 bar (T = 523 K, H_2:CO_2 = 3, flow direction in membrane–integrated cases: co–current) 43

Figure 4.5. Effect of reaction and permeate channel inlet velocities on CO_2 conversion at 10 bar (T = 523 K, H_2:CO_2 = 3, flow direction in membrane–integrated cases: co–current).. 44

Figure 4.6. Effect of reaction and permeate channel inlet velocities on converted CO_2 amount at 10 bar (T = 523 K, H_2:CO_2 = 3, flow direction in membrane–integrated cases: co–current)..... 45

Figure 4.7. Effect of reaction and permeate channel inlet velocities on CO_2 conversion at 15 bar (T = 523 K, H_2:CO_2 = 3, flow direction in membrane–integrated cases: co–current).. 46

Figure 4.8. Effect of reaction and permeate channel inlet velocities on converted CO_2 amount at 15 bar (T = 523 K, H_2:CO_2 = 3, flow direction in membrane–integrated cases: co–current)..... 47

Figure 4.9. Effect of reaction channel inlet velocity and pressure on syngas composition (T = 523 K, H_2:CO_2 = 3, permeate channel inlet velocity: $6v^{p}_{rxn,c}$, flow direction in membrane–integrated cases: co–current).. 48

Figure 4.10. Effect of H_2:CO_2 ratio on syngas composition (T = 523 K, permeate channel inlet velocity: $6v^{p}_{rxn,c}$, flow direction in membrane–integrated cases: co–current)..... 49

Figure 4.11. Comparison between multichannel and packed-bed reactors (T = 523 K, P = 5 bar, H_2:CO_2 = 3, permeate channel inlet velocity: $6v^p_{rxn,c}$, flow direction in membrane–integrated cases: co–current)..... 50

Figure 4.12. The effect of feed stream H_2:CO_2 ratio on CO_2 conversion at 5 and 15 bar (T = 523 K, permeate channel inlet velocity: $6v^p_{rxn,c}$, flow direction in membrane–integrated cases: co–current). 51

Figure 4.13. The effect of co- and counter-current permeate channel flows on CO_2 conversion at 5 and 15 bar (T = 523 K, permeate channel inlet velocity: $6v^p_{rxn,c}$).....53

LIST OF TABLES

Table 2.1. Kinetic parameters for the 3 reaction mechanisms. 17

Table 2.2. Kinetic parameters. 18

Table 2.3 Kinetic parameters. 18

Table 2.4. Kinetic parameters. 19

Table 2.5. Water adsorption capacity of FAU-13X adsorbent. 20

Table 2.6. Adsorption kinetic parameters for FAU-13X. 21

Table 2.7. Ideal gas permselectivity values of the components. 22

Table 2.8. Kinetic parameters of RWGS and Sabatier reactions. 24

Table 2.9. Experimental data of the permselectivities. 26

Table 3.1. Default values and ranges of the operating parameters for multifunctional reactor. 31

Table 3.2. Reaction parameters. 32

Table 3.3. Gibbs free energy coefficients [60] 33

Table 3.4. Properties of CZA catalyst [16, 54]. 34

Table 3.5. Model equations regarding multifunctional reactor (FP: Fluid phase, PZ: Porous Zone, ML: Membrane Layer). 38

LIST OF SYMBOLS

C_i	Concentration of species i (kmol m^{-3})
C_T	Concentration of active sites of fresh catalysts (mol g_{cat}^{-1})
$c_{p,i}$	Heat capacity of species i (J kg^{-1} K^{-1})
$c_{p,m}$	Heat capacity of gas mixture (J kg^{-1} K^{-1})
d_p	Particle diameter (m)
E_A	Activation Energy (kJ mol^{-1})
F_P	Pressure correction factor
F_i	Molar flow rate of the component i (mol s^{-1})
$G_{f,i}$	Gibbs free energy of formation of species i (kJ mol^{-1})
$H_{f,i}$	Enthalpy of formation of species i (kJ mol^{-1})
H	Height of the microchannel (m)
I	Identity matrix 3x3
J_i	Mass flux (mol m^{-2} s^{-1})
k_{eff}	Effective thermal conductivity of gas mixture in the washcoat layer (W m^{-1} K^{-1})
K_{eq}	Reaction equilibrium constant
K_i	Adsorption/desorption equilibrium constant for species i (bar $^{-1}$)
k_i	Reaction rate constant for reaction (mol kg_{cat}^{-1} s^{-1})
k_m	Thermal conductivity of gas mixture (W m^{-1} K^{-1})
k_w	Thermal conductivity of the membrane layer, (W m^{-1} K^{-1})
L	Length of the microchannel (m)
L_{edge}	Edge length of a mesh cell (m)
M_e	Weight uptake at equilibrium (g)
M_i	Molecular weight of species i (kg mol^{-1})
M_t	Weight uptake at time t (g)
n_i	Number of moles of species i (mol)
P	Pressure (bar)
P_i	Partial pressure of species i (bar)

$Perm_i$	Membrane permeability of species i (mol m^{-2} s^{-1} Pa^{-1})
R	Ideal gas constant (8.314 J mol^{-1} K^{-1})
r_{asc}	Associative mechanism reaction rate (mol h^{-1} g_{cat}^{-1})
r_{pow}	Power law expression reaction rate (mol h^{-1} kg_{cat}^{-1})
r_{redox}	Redox mechanism reaction rate (mol h^{-1} kg_{cat}^{-1})
$S_{f,i}$	Entropy of formation of species i (kJ mol^{-1} K^{-1})
S_i	Mass source term of species i (kg m^{-3} s)
T	Temperature, (°C)
$\vec{v}$	Velocity vector, (m s^{-1})
W	Width of the microchannel (m)
W_{cat}	Catalyst weight (g)
ΔG_{rxn}	Gibbs free energy of reaction (kJ mol^{-1})
ΔH_{rxn}	Heat of reaction (kJ mol^{-1})
ε_{cat}	Porosity of catalyst
μ_m	Average gas mixture viscosity, (kg m^{-1} s)
μ_i	Viscosity of species, (kg m^{-1} s)
ρ_m	Density of gas mixture (kg m^{-3})
α	Partial pressure order of CO_2
β	Partial pressure order of H_2
δ	Partial pressure order of H_2O
γ	Partial pressure order of CO

LIST OF ACRONYMS/ABBREVIATIONS

1D	One Dimensional
2D	Two Dimensional
3D	Three Dimensional
BET	Brauner-Emmett-Teller
CO	Carbon Monoxide
CO_2	Carbon Dioxide
FP	Fluid Phase
FTIR	Fourier Transform Infrared Spectroscopy
HAADF-STEM	High Angle Annular Dark Field Scanning Transmission Electron Microscopy
H_2	Hydrogen
H_2O	Water
ML	Membrane Layer
RWGS	Reverse Water-Gas Shift
SEM	Scanning Electron Microscopy
TEM	Transmission Electron Microscopy
TGA	Thermogravimetric Analysis
TPD	Temperature Programmed Desorption
TPSR	Temperature Programmed Surface Reaction
XPS	X-Ray Photoelectron Spectroscopy
XRD	X-Ray Diffraction

1. INTRODUCTION

The energy demand is increasing dramatically with the rapidly enlarging population. Since the beginning from the 20th century the population of our world has raised from approximately 1.7 to 7.8 billion people [1]. Even though recent sustainable energy technologies are being developed, mostly fossil fuels like coal, oil and natural gas are being used to meet the current energy demand. This situation causes some serious environmental problems such as high carbon emissions, greenhouse effect, climate change and ocean acidification [2]. Increasing economic growth brings an increasing energy demand as well. Global GDP is estimated to grow about 75% from 2015 to 2030, thus through 2030 it is expected that total energy demand will increase significantly [3]. To meet with this rising demand, energy production is elevated over years. This increase is expressed Figure 1.1.

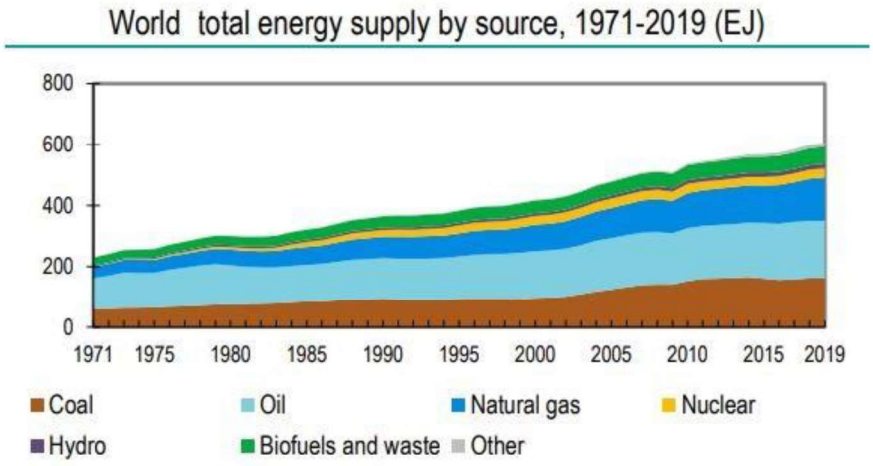

Figure 1.1. World total energy supply by source between 1971 and 2019 [4].

In year 2019, almost 3 quarters of the total energy produced was from fossil-based fuels. Even though the capacity of renewable energy technologies is increasing, it is not in a decent level yet. Non-fossil-based technologies are mainly nuclear, hydro, wind and solar type. Renewable energy technologies need to be developed to become more sustainable while outputting the sufficient amount of energy. In order to achieve the ultimate goal of environmental remediation, the technologies which are being developed has to focus more on carbon capturing and utilisation to become carbon neutral or negative [4].

Recently, technologies focusing on transforming the excess CO_2 in the atmosphere into value-added chemicals are receiving considerable interest. Capturing and utilizing abundant CO_2 in atmosphere as a chemical feedstock reduces the greenhouse effect as well as provides an alternative approach for sustainable energy technologies [5]. Carbon capture and utilization technologies (CCU) differ from carbon capture and storage (CCS) technologies with preventing from the one of the major problems of CCS which is leakage [2]. In this respect, CO_2 valorization decreases the industrial footprint while contributing to circular economies [6]. Among several CO_2 utilization routes, the reverse water-gas shift (RWGS) reaction involves catalytic hydrogenation of CO_2 to produce CO and H_2O. CO_2 is used as a C-block feedstock to produce value added-chemicals. Catalytic conversion of CO_2 into CO is an important intermediate step for many CO_2 hydrogenation process like Sabatier reaction, Fischer-Tropsch synthesis and production of methanol and dimethyl ether (DME) [7].

There are 3 major routes to produce hydrogen needed for transforming CO_2. These routes are catalytic steam/dry reforming or partial oxidation of natural gas, H_2O electrolysis and biomass gasification [8]. Carbon footprint of the RWGS reaction can be decreased by using green hydrogen which is produced from electrolysis. The electricity used in the electrolysis process can be harvested from the sun by using solar panels or from wind by using turbines.

Syngas consists of carbon oxides (CO, CO_2) and H_2. It is an important feedstock for chemical industry to produce value-added chemicals. Currently, syngas is produced by autothermal reforming or partial oxidation of natural gas, both of which are energy intensive and have notably high carbon footprints. Moreover, these technologies are suited for large scales and fall below their break-even points at low capacities [9]. These issues can be resolved by making syngas by RWGS [10]. As summarized above, conversion of CO_2 with green H2 offers syngas production with a significantly reduced carbon footprint.

Due to endothermic nature of RWGS reaction, operating temperature plays a key role on CO_2 conversion. In addition, the reaction is thermodynamically limited that even though the equilibrium constant increases with the elevating temperature the reaction rate converges to a limit value at some point. Excess feed of H_2 inlet and temperature increase affects the reaction positively [11]. CO_2 hydrogenation can result in 2 different ways, producing CO and H_2O also

known as RWGS reaction and CH_4 with H_2O can be produced, this is called Sabatier reaction. Sabatier reaction is exorthermic, therefore thermodynamically favored at lower temperatures (250-350°C). On the other hand, RWGS reaction is thermodynamically promoted at higher temperatures (600-700°C) [12]. The challenge is to carry out RWGS reaction effectively at lower temperatures. This challenge is addressed in the present study by the application of *in-situ* steam separation. The catalyst type is also crucial in addressing this challenge. In general, metal oxide supported precious metal catalysts are preferred because of their high catalytic activity, thermal stability and CO selectivity. On the other hand, precious metals are expensive in contrast with transition metals. This situation creates an inconvenience in terms of economic feasibility of the process. Precious metals such as Pt, Pd and Au are most favored with combination of metal oxides such as TiO_2, Al_2O_3 and CeO_2. Transition metals are economically feasible compared to precious metals but have lower catalytic activity, less stability and higher tendency to sintering. Among the transition metals, Ni shows relatively high catalytic activity but it is selective to methanation. As an alternative, Cu loading on reducible supports demonstrates high thermal stability and catalytic activity due to strong interaction between Cu and support [10].

Physically separating steam from the reactive medium thermodynamically enhances the RWGS reaction towards products side. Effective separation of steam, the product of RWGS, is one of the crucial problems in industries for CO_2 utilization [13]. There are two main strategies for *in-situ* steam separation: integrating a steam selective membrane or adsorbent. While steam selective membranes offer continuous separation of H_2O from the reaction medium, hydrophilic adsorbents need to be regenerated periodically for their re-use. Separating steam continuously competitively favors steam selective membrane as combining reaction and separation process in one unit and constructing process intensification [13,14]. Sodalite (SOD) and ZSM-5 are examples of steam selective membrane materials. In contrast with other steam selective membranes, SOD has relatively higher H_2O permeability and offers H_2 transfer which is important for this study in the sense that H_2 is used as a sweep gas to enhance reactor performance.

A typical microchannel reactor consists of parallel channels with dimensions in a range of 10^{-6} m to 10^{-3} m. Isothermal conditions can be obtained with microchannel reactors in addition to negligible pressure drop. Compared to conventional packed-bed reactors surface

area/volume ratios of microreactors are almost 1000 times higher, this case leads to superior contact area between the fluid and the membrane which is beneficial for membrane mass transfer. Microreactors can be easily scaled-up in terms of capacity by altering the number of channels [15]. Their architecture also allows decoration of higher membrane surface area per unit volume.

Investigation of RWGS as a promising route for syngas production forms the scope of the current study. Considering the limitations of the RWGS, it is particularly aimed to overcome the thermodynamic barrier by means of coupling the catalytic reaction with membrane separation. The reactor is selected as a microstructured unit for its relatively higher surface areas for catalysis and membrane operation. The entire flow, reaction and separation phenomena are modeled and simulated under ANSYS platform. The model is used for studying the effects of pressure, reaction channel inlet velocity, sweep velocity, inlet feed H_2:CO_2 ratio and flow partitioning on reactor performance.

This thesis is composed of five chapters. Chapter 1 is the introduction to studied areas and motivation for this study. Comprehensive literature survey about RWGS reaction including thermodynamics, catalysts and reaction kinetics in addition to process intensification are presented in Chapter 2. Modeling of the microchannel system is elucidated with description of reactor geometry, related reaction network with kinetic and membrane models, operating parameters and solution methodology in Chapter 3. Performance of the microchannel system is presented and discussed in Chapter 4. Lastly, in Chapter 5, key conclusions obtained from the studies with recommendations for future improvements are provided.

2. LITERATURE SURVEY

2.1. Reverse Water-Gas Shift Reaction

Syngas, consisting of CO, CO_2 and H_2 gases, is known for its importance regarding synthesizing synthetic fuels *via* Fischer-Tropsch mechanisms. Syngas is predominantly produced through hydrocarbon reforming processes or biomass gasification. By using RWGS reaction it is possible to valorise excess CO_2 in atmosphere to produce syngas. During RWGS reaction CO_2 hydrogenated equimolarly to being converted into more reactive CO and H_2O. The reaction is expressed as [16]

$$CO_2 + H_2 \rightleftharpoons CO + H_2O \qquad \Delta H°=41.1 \text{ kJ mol}^{-1}. \qquad (2.1)$$

Due to its mildly endothermic nature the reaction equilibrium constant increases with respect to elevating temperatures. The reaction is favored at high operating temperatures (600-700°C) that this condition causes some economic and material-based problems. While heating the reaction channel to the desired levels brings excessive costs, from the material science point of view it is challenging to find materials in the context of the process with also considering the prices of materials. In addition, steam is produced as an unwanted by-product, unless it is not physically separated from the reaction medium it can deactivate the catalyst and prohibit the reaction to move forward [17]. In this context, steam must be separated from the reaction channel. For continuous separation of the by-product, steam selective membranes can be used. These membranes allow reaction and separation to be in the same unit that allows process intensification which can be done effectively in microchannel reactors.

2.1.1. Thermodynamic Analysis

Thermal design and optimization are crucial for RWGS reactors. In this context a comprehensive thermodynamic analysis is investigated in the study of Sun *et al*. [18]. The irreversibility of heat transfer, chemical reaction and viscous flow are studied based on

entropy generation method. The total entropy generation rate (EGR) is minimized with respect to a base case scenario by optimal control theory.

Selected base case operating parameters are T=600°C, P=1MPa and mole fractions of inlet components (CO_2, H_2, CO, H_2O) are 0.45,0.45,0.05,0.05 respectively. The reactor length is reported as 5 m. By optimizing the reservoir temperature profile, inlet feed gas temperature and the reactor length concurrently a sharp EGR reduction up to 23% is succeeded compared to the reference reactor which is operating at base case conditions. This reduction is majorly caused by optimization at the heat transfer irreversibility. In addition to the heat transfer optimization, a shorter reactor length (0.41m) is selected in the successful scenario. It is observed that reactor length plays a critical role in optimization of EGR. Based on these considerations an optimum reactor is designed for commercial scenarios.

2.1.2. Catalysts and Reaction Kinetics

RWGS reaction have been studied on various catalysts and re-gained its importance with the development of carbon utilization technologies. The RWGS favored catalyst must show great thermal stability accompanied by high CO_2 conversion and CO selectivity. To achieve these criteria numerous catalyst combinations have been investigated. The catalysts can be categorized according to the type of active metal. Precious metals are generally preferred because of their higher catalytic activity and notable thermal stability. However, there is a trade-off in terms of economics and catalytic performance because that precious metals are generally expensive. On the other hand, transition metals are cheaper and easier to access but they lack thermal stability and have lower catalytic performance. To break this trade-off and optimize these properties several catalyst combinations are studied.

2.1.2.1. Precious Metal Based Catalysts

The work of Zhao *et al.* [19] focused on the effects of atomically dispersed Pt/CeO_2 catalyst on CO selectivity which is one of the major drawbacks of Pt-based catalysts. Despite the high catalytic activity of Pt-based catalysts and their high thermal stability, moderate CO selectivity is a disadvantage for the RWGS reaction. In this study, Pt is dispersed with different particle sizes on ceria and examined between the temperatures of 200-450°C. The studied

samples are 1%Pt/CeO_2-IMP-350, 5%Pt/CeO_2-IMP-350 and 1%Pt/CeO_2-AA-350. Here, IMP and AA codes represent the synthesis methods of the catalysts; IMP coded catalysts are formed with impregnation method while AA coded catalyst is formed with the proposed pre-reduction method by the authors. Synthesized catalysts are characterized by powder x-ray diffraction (XRD), the high-angle annular dark-field scanning transmission electron microscopy (HAADF-STEM), X-ray photoelectron spectroscopy (XPS), Fourier transform infrared spectroscopy (FTIR) and temperature programmed desorption (TPD) techniques. Results show that atomically dispersed Pt/CeO_2 catalyst exhibits almost 100% CO selectivity in the lower end of the given operating temperatures. With the 50°C increments through 450°C, the relation between of CO selectivity between the investigated catalysts are 1%Pt/CeO_2-AA-350 > 1%Pt/CeO_2-IMP-350 > 5%Pt/CeO_2-IMP-350. The successful catalyst exhibited 98% CO selectivity at 450°C.

Chen *et al.* [20] studied catalytic performance of Pt/TiO_2 catalyst and selectively manipulating the product formation. In the context of this study, series of experiments are done to investigate the effect of particle size on the CO_2 hydrogenation reaction and on the formation of CO rather than CH_4. The catalysts, 0.1% Pt/TiO_2, 0.5% Pt/TiO_2, 1% Pt/TiO_2, 2% Pt/TiO_2 and 5% Pt/TiO_2, are studied at the temperature range between 250 and 400°C. The effect of space velocity is also examined. The catalysts are characterized by XRD, HAADF-STEM and FTIR. The study shows that methanation reaction is favored on the large Pt particles rather than small particles. In addition, with the increasing space velocity (higher than 108000 mL g_{cat}^{-1} s^{-1}), RWGS reaction occurrence has not been affected seriously. On the other hand, methanation reaction suffered major catalytic performance loss. Both the effect of Pt particle size and space velocity are investigated thoroughly in this work.

Bobadilla *et al.* [21] studied the reaction mechanism of RWGS *via* using Au/Al_2O_3 and Au/TiO_2 catalysts. Catalytic performance of both catalysts are investigated at the temperature range of 250-450°C with a H_2:CO_2 ratio of 4. Au/TiO_2 catalyst studied in the space velocity range of 12000 to 40000 h^{-1} while Au/Al_2O_3 catalyst is studied only at 12000 h^{-1}. Results of the tests shows that Au catalyst exhibits higher catalytic activity in terms of CO_2 conversion with TiO_2 support on the contrary of Al_2O_3 support. While Au/TiO_2 catalyst almost exceeds 40% CO_2 conversion level Au/Al_2O_3 catalyst could not exhibit CO_2 near to 20% conversion. Reaction mechanism of RWGS is investigated by studying the role of oxygen vacancies on the

catalysts by means of Operando DRIFTS and UV spectroscopy. It is observed that reaction is moving forward through production of formate intermediates which are reduced to CO form in Au/Al_2O_3 catalyst. During the time, for the Au/TiO_2 catalyst, the reaction advances with production of hydroxycarbonyl intermediates and then a decomposition of those intermediates into CO, thus with the use of the catalyst redox mechanism dominates the reaction.

Nelson *et al.* [22] investigated Pd/TiO_2 catalyst for RWGS reaction while dispersing Pd atomically on TiO_2. Four different catalysts containing different weight of Pd are studied, 0.01% Pd/TiO_2, 0.02% Pd/TiO_2, 0.05% Pd/TiO_2 and 0.1% Pd/TiO_2 respectively. The catalytic performance tests are made at 400°C and atmospheric pressure, with a H_2:CO_2 ratio of 4. Helium is used as inert and carrier gas in this set of experiments having a flow rate of 10 ml min^{-1}. Extended X-ray absorption fine structure (EXAFS), scanning transmission electron microscopy (STEM) and infrared (IR) spectroscopy techniques are used characterize the studied catalysts. As outcome of the experiments, 0.01% Pd/TiO_2 catalyst showed highest catalytic activity by 5 mmol g_{Pd} s^{-1} CO formation and the 0.1% Pd/TiO_2 catalyst exhibited the lowest CO formation as just below of 2 mmol g_{Pd} s^{-1} . Due to the endothermic nature of the reaction it is aimed to develop catalysts which are thermally stable at high temperatures. The thermodynamic stability of the studied catalysts is because of enthalpic stabilization of oxygen vacancy sites are occurred during RWGS reaction.

2.1.2.2. Non-Noble Metal Based Catalysts

There are numerous probabilities to construct a catalyst but considering the importance of being economically feasible the precious metals are hard to obtain and expensive to purchase. As alternatives, Cu, Fe, Co and Ni can be used as a catalyzing metal for RWGS. Easa and O'Brien [23] studied CuO_x / SiO_2 dot core and rod shell catalyst to improve one of the major disadvantages of metallic copper-based catalysts which is thermal stability. Metallic copper-based catalysts exhibit great catalytic activity against CO_2 conversion reactions and poses high selectivity on the other hand they lack thermal stability due to agglomeration of Cu particles. In this study, crystal engineering strategy is applied to produce CuO_x/SiO_2 catalysts while process is being controlled and manipulated. Four different catalysts were synthesized to investigate the CuO_x/SiO_2 group of catalysts, two of them were synthesized from $NH_3 \cdot H_2O$ and the rest were from Na_2SiO_3 with different procedures to examine the crystal formation.

Catalysts are named as CuSiO-I, CuSiO-II, CuSiO-III and CuSiO-IV, and characterized by XRD, SEM, ICP-OES, TEM, XPS and BET methods. The experiments were done at 550-600°C with a space velocity range of 375000 to 3000000 ml g^{-1} h^{-1}. At 600 °C, CuSiO-I and CuSiO-II shows similar conversions beating CuSiO-III and CuSiO-IV by ~10%. CuSiO-III catalyst showed the lowest CO_2 conversion by ~3%. To examine thermal stability of the catalysts, catalysts were investigated at 600 °C for 45 hours. The highest catalytic activity showing catalyst, CuSiO-I demonstrated relatively great stability in the range of 45 hours and terminated its CO_2 conversion near 8%. On the contrary of its low catalytic performance CuSiO-III demonstrated excellent stability with a loss of CO_2 conversion by only 1%.

Zhou *et al.*[10] investigated supported mesoporous Cu/$CeO_{2-\delta}$ catalyst for RWGS reaction. Seven different catalysts are studied regarding their Cu load; 1 wt% Cu/$CeO_{2-\delta}$, 3 wt% Cu/$CeO_{2-\delta}$, 5 wt% Cu/$CeO_{2-\delta}$, 8 wt% Cu/$CeO_{2-\delta}$, 10 wt% Cu/$CeO_{2-\delta}$, 12 wt% Cu/$CeO_{2-\delta}$ and 15 wt% Cu/$CeO_{2-\delta}$. The catalysts are charaterized by H_2-TPR, XRD, BET, *in-situ* XPS and AAS techniques. Catalytic activity tests are done at temperature range of 240 to 400°C. In terms of CO_2 conversion, the most active catalyst was observed as 8 wt% Cu/$CeO_{2-\delta}$ with a 1.8 mmol g_{cat} min^{-1} CO_2 conversion rate. The second and third most active catalysts were 5 wt% Cu/$CeO_{2-\delta}$ and 10 wt% Cu/$CeO_{2-\delta}$, respectively. This trend shows that Cu loading amount has an optimized point and while going through the highest and lowest Cu loaded catalysts the catalytic performance reduces. The lowest CO_2 conversion is demonstrated from 1 wt% Cu/$CeO_{2-\delta}$ with a 1.0 mmol g_{cat} min^{-1} CO_2 conversion rate. In addition, the CO selectivity of the catalysts were also studied in this work. The highest CO selectivity was achieved by 8 wt% Cu/$CeO_{2-\delta}$ catalyst with 95% and with 80% the least CO selectivity is exhibited by 1 wt% Cu/$CeO_{2-\delta}$ catalyst. Considering the catalytic performances of the catalysts in terms of CO_2 conversion and CO selectivity, 8 wt% Cu/$CeO_{2-\delta}$ catalyst is observed as the most successful one.

Zhang *et al.* [24] studied Cu-CeO_2-hollow nanosphere catalysts and the role of oxygen vacancies. 3-D printed CeO_2 were prepared in hollow nanosphere, nanoparticle and nanocube morphologies to support Cu particles, they were denoted as Cu-CeO_2-hs, Cu-CeO_2-np and Cu-CeO_2-nc respectively. The prepared catalysts are characterized by *in-situ* DRIFTS, *in-situ* UV-Raman, SEM, TEM, XRD and TPR methods. The catalysts examined under the temperature range of 250-600°C, with a H_2:CO_2 ratio of 3 and weight hourly space velocity (WHSV) is fixed to 300,000 mL g^{-1} h^{-1}. Among 3 different configurations, Cu-CeO_2-hs catalyst exhibit the

best catalytic performance by almost 50% CO_2 conversion. The least successful catalyst in terms of CO_2 conversion was Cu-CeO_2-nc catalyst with ~15%. In addition, catalytic activities are also measured in terms of mmol g^{-1} s^{-1}. As Cu-CeO_2-hs catalyst showed the highest CO_2 conversion its thermal stability is examined with a 30 hour long test. At the end of the test, conversion of the catalyst decreased from 50% to 35%, it demonstrated a linear reduction through time. Furthermore, this study outputted that the particle size of Cu was not the rate determining factor and the oxygen vacancy quantity was directly proportional with catalytic reaction rate.

Chen *et al*. [25] investigated the catalytic performance of Cu-Fe/CeO_2 bimetallic catalyst. The combinations in terms of active metal loadings were 10% Cu-CeO_2, 15% Cu-CeO_2, 20% Cu-CeO_2, 5% Cu-5%Fe/CeO_2, 10% Cu-5%Fe/CeO_2 and 15% Cu-5%Fe/CeO_2 catalysts. Cu and Fe are extremely dispersed on CeO_2 support to construct Cu-Fe/CeO_2 bimetallic catalyst. The experiments were done at a temperature range of 450-750°C and H_2:CO_2 ratio of 1. The synthesized catalysts characterized by BET, SEM and TPO techniques. Catalytic performances of the catalysts were assessed in terms of CO_2 conversion. Among iron free synthesized catalysts, the highest performance was demonstrated by 15% Cu-CeO_2. It is observed that addition of Fe particles to the catalysts highly increased CO_2 conversion at the mid-temperatures (450-600°C) of the range. The conversion increased from near 15% to almost 35%, this increase is mentioned between 10% Cu loaded catalysts. In addition to the elevation in catalytic performance with the addition of Fe particles to the Cu-based catalyst thermal stability of the previous catalyst improved significantly. During 48 hour long thermal stability tests, CO_2 conversion of the 10% Cu loaded catalyst oscillated between 40% and 45% starting from 42% and ending at 40%. Throughout the experiments by-product formation was negligible. Also, no carbon deposits were detected on the bimetallic catalyst. It is monitored that CO_2 conversion almost reached its thermodynamic limit.

Bahmanpour *et al.* [26] focused on developing a novel Cu-based catalyst due their high catalytic activity and selectivity. To overcome one of the major drawbacks of the Cu-based catalysts which is thermal stability, the authors discussed addition of aluminum to form a Cu-Al spinel catalyst. The catalyst, prepared by the co-precipitation method, exhibits the highest catalytic performance among all Cu-based ones. 4Cu-Al_2O_3 and Cu/Al_2O_3 catalysts were examined and 4Cu-Al_2O_3 catalyst showed 47% CO_2 conversion at 600°C, WHSV=300,000 mL

g^{-1} h^{-1} while Cu/Al_2O_3 catalyst was just above 10%. Even at this high WHSV, no significant deactivation was observed. During 40 hour long thermal stability test the catalyst showed remarkable performance against high temperature. Regarding the literature, it is reported that high Cu loadings leaded to reduction in catalytic activity and stability. On the contrary, it is stated in the study that $4Cu\text{-}Al_2O_3$ catalyst is one of the important candidates for RWGS reaction. The spinel catalysts were characterized by BET, BJH, TPR and ICP-OES techniques.

Jurkovic *et al.* [27] investigated the effect of different type of supports on Cu-based catalysts. Five different catalysts were studied with Al_2O_3, CeO_2, SiO_2, TiO_2, and ZrO_2 supports on 10% Cu. Series of experiments are carried out at temperature range between 280 to 360°C with a WHSV varying from 0 to 0.1 g_{gas} $gcat^{-1}$ min^{-1}. Regarding to the effect of temperature, it is observed that Cu/Al_2O_3 demonstrated the best catalytic performance in terms of product concentration (vol%CO). The weakest performance is shown by Cu/ZrO_2 through this range. In addition to the effect of the temperature, the effect of pressure was also evaluated. Pressures of 3 bar and 7 bar were studied. While Cu/SiO_2 and Cu/CeO_2 catalysts almost demonstrate the same product concentrations at the studied pressures, Cu/TiO_2 catalyst is significantly affected by the pressure increment in a positive way. With the increasing pressure, product concentrations showed a great result and almost folded. Furthermore, the effect of H_2:CO_2 ratio is examined at 0.67, 1 and 1.5 values. The increase in the ratio affected Cu/CeO_2 most positively among the other catalysts. While the ratio was increased from 0.67 to 1.5, Cu/CeO_2 was raised from the second-best catalytic performance to the top performance eliminating Al_2O_3 support. Also, ZrO_2 and SiO_2 supported Cu catalysts exhibited almost the lowest product concentrations for the studied H_2:CO_2 ratios. Lastly, TiO_2 supported catalyst ranked as 3rd according to the operated parameters.

Liu *et al.* [28] investigated partially sintered $Cu\text{-}CeO_2$ catalyst due to it's high potential of catalytic activity and selectivity with a great thermal stability at high temperatures. To complete the aimed experiments four different catalysts containing 5CuCe, 15CuCe, 15CuAl and CeO_2 with varying ratios were studied at a temperature range of 300 to 600°C. At atmospheric pressure H_2:CO_2 ratio was selected as 4 and a high space velocity of 400000 mL $gcat^{-1}$ h^{-1} was operated. 15CuCe catalyst showed great catalytic performance in terms of CO_2 conversion, it had almost reached to the thermodynamic limit of the RWGS reaction at 600°C by just above 55%. CeO_2 was the least successful catalyst by far at the studied intervals of

temperatures, it exhibited 8% CO_2 conversion at 600°C. To examine the thermal stability of the catalysts, 240 h long stability tests were made at 600°C and 400000 mL $gcat^{-1}$ h^{-1}. 15CuCe catalyst was again demonstrated the best performance regarding thermal stability at high temperature. It showed only an insignificant decrease until 20 h, after passing the 20 h barrier until 240 h it was shown highly stable. It is reported in this study that this insignificant deviation of the stability is caused because of minorly sintering of CeO_2. Also, besides it's high conversion and stability, 15CuCe catalyst was 100% selective against CO. The catalysts are characterized by BET, TEM, DRIFTS and TPSR.

Pastor-Perez *et al.* [29] focused on developing Cs-doped Fe-Cu/Al_2O_3 catalyst for CO_2 utilization strategies. To better understand the contribution of catalysts components Fe/Al_2O_3, Fe-Cu/Al_2O_3, Fe-Cs/Al_2O_3 and Fe-Cu-Cs/Al_2O_3 were investigated thoroughly. The catalysts were synthesized by wet impregnation method and characterized by XRD and XRF techniques. The experiments were made at the temperature range of 400 to 750°C at atmospheric pressure with a H_2:CO_2 ratio of 4. The system is operated at a weight hourly space velocity of 12500 mL g^{-1} h^{-1}. The results showed that regarding CO_2 conversion performances of the catalysts, starting from the basis catalyst which contains only Fe as active metal. Fe/Al_2O_3 catalyst exhibited a weak catalytic activity at lower temperatures compared to other scenarios. Separately addition of Cu or Cs to the catalyst both affected the CO_2 conversion almost the same in a favorable way. Doping the Fe-Cu/Al_2O_3 catalyst with Cs significantly increased the catalytic performance especially below 600°C. It is observed that at 750°C all catalysts reached to the thermodynamic limit of the reaction due to the endothermic nature of the reaction. Unlike the other catalysts in this study, Fe-Cu-Cs/Al_2O_3 is reported as 100% selective for all the studied temperature range. The least CO selective catalyst in this study was Fe-Cu/Al_2O_3 with near 90% selectivity. In addition, the effect of WHSV was investigated with a range of 6250 to 25000 mL $gcat^{-1}$ h^{-1}. It is stated that the CO_2 conversion was increased with the increasing WHSV, but this increase was not created a huge difference between the cases. Lastly, thermal stability of the Fe-Cu-Cs/Al_2O_3 catalyst were examined at 500°C and 12500 mL $gcat^{-1}$ h^{-1} for 50 hours. The catalyst was found to highly stable over the examination duration and preserved its catalytic performance including minor loses.

Ronda-Lloret *et al.* [30] focused synthesizing CuO_x/CeO_2 catalyst by novel alternative technique and the comparison of the method with the conventional method. According to the authors the most common synthesis method for CuO_x/CeO_2 catalysts is wet impregnation method. In this study the catalyst is formed by using metal organic frameworks (MOF) as precursors. As the new techniques discussed in the work, Cu-MOF was firstly impregnated with CeO_2 precursor then pyrolyzed the impregnated MOF with series of varying operating conditions. The synthesized catalyst was characterized by XRD, XPS, Raman and TPR methods. According to the results of the comparison of MOF-derived catalyst and the catalyst produced with wet-impregnation method, the developed catalyst in this study moderately exhibits better catalytic performance in the operating temperature range of 260 to 340°C. Thermal stability tests were run over 20 h, at it is observed that the catalyst shows fairly good stability at the beginning. On the other hand after a duration of 10 h the catalysts started to be deactivated in sluggishly. In addition, it is stated that pyrolysis conditions such as temperature and atmosphere type (inert N_2 or air) were extremely crucial on the production processes of the investigated catalyst.

He *et al.* [31] investigated support-free MnO_x nanostructures as the catalyst for RWGS reaction and their morphology. Manganese oxides which formed as 1-D, 2-D and 3-D nanostructures showed great selectivity (100%) to CO and at high temperatures (850°C) the catalyst exhibited strong thermal stability while performing high catalytic performance in terms of CO_2 conversion up to 50%. The experiments were made at a temperature range between 400 to 850°C, atmospheric pressure and H_2:CO_2 ratio of 1. Synthesized 1-D, 2-D and 3-D MnO_x catalysts were compared with a commercial MnO_2 catalyst. Regarding the results of the study, 2-D MnO_2 nanosheets performed highest CO_2 conversion reaching up to 50% and 1-D α-MnO_2 nanowires showed almost similar catalytic activity to the 2-D nanosheet catalyst. While 3-D ε-MnO_2 nanoflower and the commercial catalysts exhibited relatively poor catalytic activity with a conversion range of 10-20%. To examine thermal stability of the catalysts, all catalysts are tested for 10 h long experiments at 850°C. 1-D nanowire catalyst showed a significant stability with almost no catalytic performance loss meanwhile 2-D nanosheet and 3-D nanoflower exhibited a slight disappearance.

Yang *et al.* [32] focused on the effect of transition metal promoters on Ni/CeO_2-Al_2O_3 catalyst. In this context four different catalysts are synthesized, NiFe/CeAl, NiCr/CeAl, Ni/CeAl and Ni/Al to investigate the impacts of the components. The synthesized catalysts are characterized by XRD, TPS and XPS techniques. The examination of the catalysts is made at a temperature range of 400-750°C, WHSV of 30,000 mL $gcat^{-1}$ h^{-1} and H_2:CO_2 ratio of 4. Results show that NiFe/CeAl catalyst demonstrate the best catalytic performance among the studied catalysts with a CO_2 conversion close to thermodynamic limit of the reaction which is near 70%. Ni/Al catalyst is the least successful regarding the catalytic activity of the studied catalyst while NiCr/CeAl and Ni/CeAl catalysts show almost similar conversions. At challenging operating conditions, stability tests of NiFe/CeAl and NiCe/Al are made, high WHSV of 400000-800000 mL $gcat^{-1}$ h^{-1} is applied to the system and temperature sustained at 750°C. For both WHSV values, NiFe/CeAl catalyst performs better stability in contrast with NiCe/Al catalyst. It is reported that Ni-FeO_x catalysts are promising for RWGS reaction because of their great catalytic performance and also for future CO_2 valorization technologies.

Peng *et al.* [33] investigated graphitic carbon supports doped with N on Co-Fe catalyst. In this study the N-doped graphitic carbon material is produced from agricultural wastes and shows significant catalytic activity. Ten samples are examined according to their catalytic performance and CO selectivity. Samples number 1,2 and 3 were the most successful catalysts with CO_2 conversions 38%, 33% and 44% respectively at 450°C. Also, these catalysts almost exhibited 100% CO selectivities. The operating conditions for catalytic performance tests were made at a temperature range of 300-500°C, 10 bar pressure, H_2:CO_2 ratio of 7 and space velocity of 600 h^{-1}. In the studied range of temperature 300-500°C, sample 1 showed the best catalytic properties with 56% CO_2 conversion and 98% CO selectivity. The catalyst named as sample 1 contains 0.042 wt% of Co and 0.053wt% of Fe with a Fe/Co ratio of 1.26 as it is 3rd top ratio among 10 samples. Other 2 samples having Fe/Co ratio more than 1.26 showed lower catalytic performance due their high Co and Fe wt% ratio. The catalysts were characterized by field emission scanning electron microscopy (FESEM), high-resolution transmission electron microscopy(HRTEM), XRD and TEM techniques.

2.1.2.3. Metal Carbide Catalysts

Ma *et al.* [34] aimed to investigate the effect of β-Mo_2C on N-doped carbon by examining different concentrations of β-Mo_2C. In this context, five different concentrations of β-Mo_2C were studied; β-Mo_2C, Mo_2C(%5)/N-C, Mo_2C(%10)/N-C, Mo_2C(%20)/N-C and Mo_2C(%100)/N-C. The synthesized catalysts were characterized by TPSR, TEM, XPS, STEM, BET, BJH, and ICP-OES. The catalytic performance tests were made at a temperature range of 240 to 600°C, H_2:CO_2 ratio of 4 and WHSV of 24,000 mL g_{cat}^{-1} h^{-1}. The results showed that Mo_2C(%10)/N-C and Mo_2C(%5)/N-C exhibited top best 2 catalytic activities with 184 and 175 μmol/g_{cat}^{-1} s^{-1} respectively. On the other hand, β-Mo_2C was demonstrated a catalytic activity of 21 μmol/g_{cat}^{-1} s^{-1}. To show the effect of H_2:CO_2 ratio, top performing sample which is Mo_2C(%10)/N-C is examined at H_2:CO_2=4, also to contrast with the base scenario β-Mo_2C is investigated at the ratio of 4. It is observed that with the increasing H_2:CO_2 ratio reaction rate was decreased from 184 to 163 μmol/g_{cat}^{-1} s^{-1} for both of the catalysts. In addition, with the higher ratio, CO selectivity slightly increased and reached 99.5%. Moreover, to analyze thermal stability of the catalysts 60 h long tests were made at 400°C and WHSV of 24,000 mL $gcat^{-1}$ h^{-1}. In these examinations, Mo_2C(%10)/N-C showed great stability in contrast with other studied catalysts.

Morse *et al.* [35] focused on catalytic performance and morphology of alkali metal promoted tungsten carbide (WC) catalyst on γ-Al_2O_3 support. The WC/ γ-Al_2O_3 catalyst was synthesized by evaporation deposition method and characterized by BET, SEM XRD, XPS and TPC methods. Na and K were selected as Alkali metals to promote the catalyst, also an unpromoted sample(WC only) was tested to see the component effects in a clearer way. The catalytic performance of the catalysts was examined for low temperature RWGS reaction at a temperature range of 300-350°C, 20 bar, H_2:CO_2 ratio of 3 and WHSV of 1.01 mL g_{cat}^{-1} s^{-1}. The results of the study indicates that unpromoted-WC performed slightly better than the both Na and K promoted tungsten carbide catalysts with CO_2 conversions of 3.8%, 1.7% and 1.4% respectively at 300°C. On the contrary of the performance losses of the catalysts, the alkali metal promoters (Na and K) significantly improved CO selectivities. Na-WC and K-WC catalysts both exhibited 100% CO selectivity. While elevation of the operating temperature towards 350°C affected the CO_2 conversion positively, fully CO selective catalysts preserved their selectivity. Lastly, thermal stabilities of the catalysts were examined at 350°C, 20 bar,

H_2:CO_2 ratio of 3 and WHSV of 1.01 mL g_{cat}^{-1} s^{-1} 120 hour long. Similar to the catalytic performance tests, unpromoted-WC outperformed the alkali metal promoted catalysts. K-promoted WC catalyst was reported as the least successful catalyst through stability tests.

2.1.2.4. Reaction Kinetics

Kim *et al.* [36] studied the impact of support's reducibility over the reaction mechanism on Pt catalysts. Al_2O_3 and TiO_2 were selected to being investigated as supports. In the context of kinetic study, redox mechanism, associative mechanism and power law were generated and contrasted with the experimental data. It is observed that the reaction was more approximate with redox mechanism for both supports. The catalytic studies were made at 623K and 3.4 atm. Regarding the results of the experiments, on the Pt/TiO_2 surface a new active site was comprised and led to higher CO_2 conversion of the catalyst than Al_2O_3 supported catalyst. The reaction rates and parameters for associative mechanism, redox mechanism and power law are expressed as

$$r_{asc} = \frac{k(P_{CO_2} P_{H_2} - (P_{CO}P_{H_2O}/K_{eq}))}{(1 + K_1P_{CO_2} + K_2P_{H_2} + (P_{CO}/K_3) + (P_{H_2O}/K_4))^2}, \quad (2.2)$$

$$r_{redox} = \frac{k_A k_B C_T (P_{CO_2} P_{H_2} - (P_{CO}P_{H_2O}/K_{eq})}{(k_A P_{CO_2} + k_{-A} P_{CO} + k_B P_{H_2} + k_{-B} P_{H_2O})}, \quad (2.3)$$

$$r_{pow} = k\,(P_{CO_2})^{\alpha}(P_{H_2})^{\beta}(P_{CO})^{\gamma}(P_{H_2O})^{\delta}. \quad (2.4)$$

Reaction rate constant is represented by k, equilibrium constant by K_{eq} and adsorption-desorption constants of the reaction components by K_i. P_i shows the partial pressures of the components for associative mechanism. For redox mechanism kinetic parameters, C_T demonstrates concentrations of vacant active sites while k_{+i} represents forward reaction constants and K_{eq} shows the equilibrium constant. Partial pressures of the reaction components are represented by P_i. For power law kinetic parameters, k is the reaction constant where P_i is the partial pressures of the reaction components and $\alpha, \beta, \gamma, \delta$ are the constants respectively.

Table 2.1. Kinetic parameters for the 3 reaction mechanisms.

	Pt/TiO_2	**Pt/Al_2O_3**
Associative Mechanism		
k ($mol^{-1}\ h^{-1}\ g_{cat}^{-1}\ atm^{-2}$)	k=0.402	k=0.308
K_1, K_2 (atm^{-1})	K_1=0.07 K_2=1.602	K_1=0.07 K_2=1.602
Redox Mechanism		
$k_A C_T$ ($mol^{-1}\ h^{-1}\ g_{cat}^{-1}\ atm^{-1}$)	$k_A C_T$=6.38 x 10^{-2}	$k_A C_T$=6.67 x 10^{-2}
$k_B C_T$ ($mol^{-1}\ h^{-1}\ g_{cat}^{-1}\ atm^{-1}$)	$k_B C_T$=5.92 x 10^{-1}	$k_B C_T$=2.89 x 10^{-1}
Power Law		
k ($mol^{-1}\ h^{-1}\ g_{cat}^{-1}\ atm^{-(\alpha+\beta)}$)	k=0.057, α=0.794, β=0.246 γ=-0.013 , δ=-0.014	k=0.052, α=0.323, β=0.702 γ=-0.028 , δ=-0.032

Wolf *et al.* [37] investigated stability of the catalyst, reaction kinetics and modeling of the proposed system for RWGS reaction by using Ni-Al_2O_3 catalyst. Effective and intrinsic rates with their proposed models were elucidated in this study. The experiments were made at a temperature range of 796-839°C, atmospheric pressure and H_2:CO_2 of 3. A comprehensive statement was made for the reaction kinetics of RWGS and it is expressed as

$$r_{CO_2,intrinsic} = r_{CO_2,intrinsic,f} - r_{CO,intrinsic}\ , \tag{2.5}$$

$$r_{CO_2,intrinsic,f} = k_{CO_2}(T)\ C_{CO_2} C_{H_2}^{0.3}\ , \tag{2.6}$$

$$k_{CO_2}(T) = k_{CO_2,0}\ e^{\frac{-E_A}{R\,T(K)}}\ , \tag{2.7}$$

$$r_{CO,intrinsic} = k_{CO_2}\left(C_{CO_2} C_{H_2}^{0.3} - \frac{1}{K_{eq}} \frac{C_{CO}\ C_{H_2O}}{C_{H_2}^{0.7}}\right), \tag{2.8}$$

$$K_{eq} = \frac{1}{e^{(-0.29353\ Z^3 + 0.63508\ Z^2 + 4.1778\ Z + 0.31688)}}, \tag{2.9}$$

$$Z = \frac{1000}{T(K)}. \tag{2.10}$$

Table 2.2. Kinetic parameters.

Parameter	Value
$k_{CO_2,0}$($m^{3.9}$ kg^{-1} s^{-1} $mol^{-0.3}$)	3100
$-E_A$(kJ mol^{-1})	82

Parra *et al.* [38] studied a novel and promising route for RWGS reaction after developing a fixed-bed adsorptive reactor in the previous work. By this novel method it is aimed to work at lower temperatures (120-300°C) with high CO_2 conversions. The author calculated the reaction rate by

$$r = k\, e^{\frac{-E_A}{R\,T(K)}}\left(y_{CO_2}y_{H_2} - \frac{y_{CO}y_{H_2O}}{K_{eq}}\right)F_P. \quad (2.11)$$

Reaction constant is represented with k and E_A is the activation energy. Also, K_{eq} symbolizes equilibrium constant of the reaction which is quantified as

$$K_{eq} = e^{\left(4.33 - \frac{4577.8}{T(K)}\right)}. \quad (2.12)$$

In order to use the Equation (2.11) up to pressure of 30 atm, pressure correction factor is defined by F_P. Pressure is in Pascal unit. Furthermore, mole fractions of the components are represented by y_i. Pressure correction factor is calculated as

$$F_P = \left(\frac{P}{10^5}\right)^{0.5 - \frac{P}{250\ x\ 10^5}}. \quad (2.13)$$

Table 2.3 Kinetic parameters.

Parameters	Value
k (mol kg_{cat}^{-1} s^{-1})	8.22 x 10^4
E_A (kJ mol^{-1})	47.4

Dzuryk and Rezaei [16] investigated a comprehensive modeling study on intensification process *via* steam selective membranes in a packed-bed reactor. The aim of this study is to integrate a hydrophilic membrane that physically separates steam from the reaction medium for promoting the forward reaction and increasing the catalytic performance of the reactor. The operating parameters for the system are 250°C and 5 bar. The authors re-evaluated the Parra *et al.*'s model according to their experimental data. The new kinetic model is shown as

$$r = k\, e^{\frac{-E_A}{R\,T(K)}} \left(y_{CO_2} y_{H_2} - \frac{y_{CO} y_{H_2O}}{K_{eq}} \right) F_P. \tag{2.14}$$

The kinetic model has the same structure with the previous version of it, on the contrary only reaction constant(k) and activation energy(E_A) had re-calculated according to the experimental data. New reaction constant and activation energy values can be found in Table 2.4.

Table 2.4. Kinetic parameters.

Parameters	**Value**
k (mol kg_{cat}^{-1} s^{-1})	2.185 x 10^5
E_A (J mol^{-1})	7.16 x 10^4

2.2 Intensification of the Reverse Water-Gas Shift Reaction

2.2.1. Sorption Enhanced Reactors

Pieterse *et al.* [39] focused on designing a new process entitled "COMAX" with bifunctional catalysts which simultaneously affect CO_2 conversion positively and separate steam from the reaction medium. In this study, active phase (Cu,Pt) was loaded on the carrier to disperse the active sites efficiently and to increase H_2O adsorption capacity. The bifunctional catalyst was fully selective against CO up to 30 bar. The experiments were made at a temperature range of 225 to 475°C and atmospheric pressure. Two different catalysts with catalytic properties were combined with two different adsorbents; in total four bifunctional catalysts (2wt%Pt,13X; 2wt%Pt,4A; 10wt%Cu,13X; 10wt%Cu,4A) were investigated. Regarding the results of the study, 2wt%Pt,13X catalyst showed the highest catalytic performance with almost achieving thermodynamic limit and demonstrated a CO_2 conversion

higher than 50% at 475°C. To exhibit the effect of adsorbent 2wt%Pt,13X is compared by 2wt%Pt,4A. It is reported that the catalyst which has 13X as a sorbent has slightly higher catalytic activity than the 4A sorbent. The comparison among Cu based catalysts also showed the same trend with a more solid way. 10wt%Cu,13X catalyst demonstrated a catalytic performance significantly higher than the 10wt%Cu,4A catalyst. In order to examine the adsorption capacity of the catalyst, 80 h long experiment was made. It was observed that the catalyst reaches the full capacity after 75 h.

Ghodhbene et al. [40] made a comprehensive study on adsorption capacity and kinetics of hydrophilic zeolite sorbents. The study is carried out in the temperature range of 25 -250°C at atmospheric pressure and investigates SOD, LTA-3A, LTA-4A, LTA-5A and FAU-13X sorbents. To determine the kinetics of adsorption, transient adsorption data is obtained and fitted with double stretched equation technique. Regarding water adsorption capacities of the adsorbents, 13X showed the highest adsorption capacity through all temperature range. The gap between the FAU adsorbent and the LTA adsorbents is closed by increasing temperature. It is reported that the temperature affects all adsorbents negatively in terms of H_2O adsorption capacity. The lowest capacity was exhibited by LTA-5A at 25°C, on the other hand with the elevation of the temperature the performance of LTA-5A improved and at 250°C LTA-3A showed the lowest capacity.

Table 2.5. Water adsorption capacity of FAU-13X adsorbent.

Form	**Temperature(°C)**	**Capacity(g/g)**	**P_{water}(kPa)**
Bead	25	0.2802	2.33
Powder	25	0.3176	2.33
Bead	50	0.2446	2.33
Bead	100	0.1897	2.33

In this study also the SOD, LTA and FAU adsorbents are compared in terms of H_2O adsorption capacities. Again, FAU-13X showed the highest adsorption capacity by far and LTA-4A demonstrated an average capacity. SOD sorbent showed the least capacity undoubtedly. Through high temperatures, SOD sorbent was highly affected by this temperature change. A model for adsorption kinetics is presented as

$$\frac{M_t}{M_e} = A_1\left(1 - e^{-(k_1 t)^{\beta_1}}\right) + (1 - A_1)\left(1 - e^{-(k_2 t)^{\beta_2}}\right). \quad (2.14)$$

Table 2.6. Adsorption kinetic parameters for FAU-13X.

Temperature(°C)	A_1	k_1	k_2	β_1	β_2
25	0.49	0.04	0.09	2.86	1.53
50	0.58	0.05	0.11	2.55	1.48
100	0.72	0.06	0.17	2.16	1.59
150	0.73	0.11	0.20	1.45	1.75
200	0.30	0.14	0.29	1.62	1.69
250	0.28	0.17	0.35	1.60	1.85

In Equation (2.14), M_t represents weight uptake at time t and M_e shows equilibrium uptake. β_i, k_i and A_1 are the kinetic parameters for adsorption and fraction contributions, respectively.

2.2.2. Membrane Reactors

Lee *et al.* [41] investigated polymide (PI) hollow fiber membranes for *in-situ* steam separation at RWGS reaction aiming to overcome the thermodynamic limit. Simultaneous separation of steam from the reaction medium enhances the forward reaction. This situation is caused by H_2O which is a by-product of this reaction acts as an inhibitor for the forward reaction and prohibits the conversion of CO_2 into CO. The permeability of the PI membrane is studied in a temperature range of 200 to 300°C. H_2O permeability of the membrane at 200°C is reported as 2 x 10^4 Barrer and with the increasing temperature the permeability also increased. At 300°C the permeability is increased to almost 6 x 10^5 Barrer. Within the same range of temperature, the permselectivity properties of the membrane are also examined. Permselectivity values of

H_2O/H_2, H_2O/CO_2 and H_2O/CO were 10^4, 2 x 10^3 and 2 x 10^2 respectively at 200°C. In addition to the permeability properties, the effect of the membrane to the catalytic performance in terms of CO_2 conversion against different steam to carbon ratios at 250, 275 and 300°C are studied. At 250°C with the integration of the steam selective membrane, thermodynamic limit was overcome and CO_2 conversion is tripled. The highest difference between the obtained CO_2 conversion and thermodynamic limit was observed at 275°C.

Lafleur *et al.* [42] investigated a novel synthesis method for zeolites, built on mechanical pore-plugging of the supports via selected sized seeds, which is followed by secondary growth with autothermal synthesis. By this new technique hydroxy-sodalite (H-SOD) membrane was formed and examined in this study. The seeds and synthesized membranes were characterized by SEM and XRD methods. Permeability of the components and permselectivity values were investigated thoroughly. Permeabilities values of the components through the membrane grown in ZrO_2/TiO_2 support were examined in a wide range of temperature(25-250°C). Permeability of H_2O was reported as the highest permeability value among all of the components with a value of almost 1 x 10^7 mol m^{-2} s^{-1} Pa^{-1} at 150°C and 1.25 x 10^7 mol m^{-2} s^{-1} Pa^{-1} at 250°C. Also, permeability of H_2 was the second best performance between the other components. CO_2 and N_2 were the least permeable components through H-SOD membrane. In addition, ideal gas permselectivity values of the components are given below in Table 2.7.

Table 2.7. Ideal gas permselectivity values of the components.

	150°C	200°C	250°C
H_2O/H_2	6.3	2.8	1.4
H_2O/CO_2	28.1	11.7	4.8
H_2O/N_2	32.5	11.6	5.1

2.2.3. Microchannel Reactors

Sohn *et al.* [43] studied modeling of RWGS reactor in a micro-structured reactor for syngas production at elevated temperatures. Some important motivations regarding this study and major advantages of microchannel reactors are high surface area to volume ratio, enhanced heat and mass transfer properties and ability to being easy scaling up. For the reaction Ni/γ-Al_2O_3 catalyst was preferred. The experiments were made at a temperature range of 600-1000°C due to the endothermic nature of the reaction at atmospheric reaction with a H_2:CO_2 ratio of 1. Additionally, the effects of inlet velocities, H_2:CO_2 ratio and channel diameter were investigated. At 800°C, H_2:CO_2=1, channel diameter=4.57 mm; different inlet velocities (1, 2, 3, 4, 5 and 10 m/s) were examined. Velocity of 1 m/s showed the highest CO_2 conversion with almost 40% and 10 m/s demonstrated the lowest CO_2 conversion as reaching 5%. This result originates from the contact time between the catalyst and the inlet stream, when the inlet velocity decreases the opportunity to contact between the catalyst and reactants arises thus catalytic performance enhances. The effect of inlet temperature was studied at the temperatures of 600, 700, 800, 900 and 1000°C at atmospheric pressure, H_2:CO_2 ratio=1, channel diameter=2 mm and inlet velocity= 3 m/s. Due to the endothermic nature of the reaction it was reported that catalytic activity in terms of CO_2 conversion increased through elevating temperature. The highest CO_2 conversion among this range was achieved at 1000°C with near 55%. Also, it was observed that higher temperatures allowed the use of shorter channel lengths. The effect of H_2:CO_2 ratio was studied at 800°C, channel diameter=2 mm and inlet velocity= 3 m/s. It was seen that increase in the ratio affect catalytic activity positively. At H_2:CO_2 ratio=3, CO_2 conversion was reported near 47% while at the H_2:CO_2 ratio=1, it is observed as almost 37%.

Engelbrecht *et al.* [44] investigated CO_2 methanation reaction (Sabatier reaction) in microchannel reactor numerically and experimentally. The reaction constants regarding the obtained experimental data were constructed for Sabatier and RWGS reactions. A commercial 8.5wt% Ru-Cs/Al_2O_3 catalyst was selected. The sets of experiments were studied at a temperature range of 250-400°C, pressure of 1, 5 and 10 bar and space velocity range of 32.6-97.8 L g_{cat}^{-1} h^{-1}. At 250°C, atmospheric pressure and 32.6 L g_{cat}^{-1} h^{-1} , while CO_2 conversion was observed under 10%, through 400°C it reached to the highest level with a conversion of 80.4%. In addition, the effect of space velocity was investigated in the range of 32.6-97.8 L g_{cat}^{-1} h^{-1}. At 400°C, it was reported that with the increasing space velocity CO_2 conversion dropped

from 80.4% to just under 50%. Thus, space velocity and CO_2 conversion were affected inversely from each other. The effect of pressure was studied under atmospheric pressure, 5 and 10 bar. At 350°C, the difference between the CO_2 conversions at 1 bar and 5 bar pressures reached to the peak point. With pressure at 1 bar CO_2 conversion was obtained near 50%, on the other hand the conversion at 5 bar was reported as almost 90%. The highest CO_2 conversion achieved was at 10 bar pressure and 400 °C with above 90% conversion. Experimental results were compared to the simulations which were made under ANSYS platform. It was reported that the experimental data and the predicted results from the simulations were matching with 97% fit. Kinetic parameter estimations for the Sabatier and RWGS reactions are presented as

$$r_{RWGS} = -A\, e^{\frac{-E_A}{R\,T(K)}}\, x\, C_{CO_2}, \tag{2.15}$$

$$r_{SB} = \frac{1}{RT}\frac{d_{P_{CO_2}}}{dt}. \tag{2.16}$$

Table 2.8. Kinetic parameters of RWGS and Sabatier reactions.

Sabatier	**Values**	**RWGS**	**Values**
1 bar		**1 bar**	
A($bar^{-2.5}$ s^{-1})	6.17 x 10^7	A(s^{-1})	2.94 x 10^7
E_A(kJ mol^{-1})	77.96	E_A(kJ mol^{-1})	89.83
n	0.85	n	-
5 bar		**5 bar**	
A($bar^{-0.92}$ s^{-1})	7.63 x 10^6	A(s^{-1})	1.76 x 10^7
E_A(kJ mol^{-1})	74.73	E_A(kJ mol^{-1})	85.94
n	0.305	n	-
10 bar		**10 bar**	
A($bar^{-0.67}$ s^{-1})	6.83 x 10^6	A(s^{-1})	3.63 x 10^6
E_A(kJ mol^{-1})	69.35	E_A(kJ mol^{-1})	77.36
n	0.222	n	-

2.2.4. Structured Membrane Reactors

Koybasi *et al.* [45] investigated parametric study on converting syngas (CO, CO_2 and H_2) into DME in a steam selective membrane integrated microchannel reactor. Structured microreactor allows to selectively separate H_2O from the reaction medium to enhance catalytic performance of the reaction, also the microreactor benefits high surface area between the hydrophilic membrane and the inlet stream. Cu-ZnO/Al_2O_3 and HZSM-5 catalysts were selected for methanol synthesis and dehydration reactions respectively. Supported sodalite (SOD) membrane was used to selectively separate steam from the reaction channel. Effects of the temperature (493-533 K), pressure(30-60 bar), CO_2/CO_x ratio, inlet velocity and hydrophilic membrane was investigated comprehensively. DME yield decreased from almost 50% to near 30% with the increasing temperature. This results originatef from the exothermic nature of the reactions. CO and CO_2 conversions were reversely affected from the temperature, while the CO conversion significantly decreases through the elevating temperature the CO_2 conversion slightly increases. It was reported that pressure affected to the DME yield positively. In addition, CO_2/CO_x was studied from 0.2 to 0.9. CO conversion was drastically dropped with the increasing ratio, also DME yield affected negatively from the ratio increase. Moreover, for the cases studied at 523 and 533 K, the impact of the membrane integration on CO_2 conversion and DME yield were significantly positive. Lastly, effect of inlet velocity was investigated through 0.01 to 0.25 m/s. It is indicated that increasing inlet velocity affects DME yield positively.

Koybasi *et al.* [46] studied one-step DME production in a hydrophilic membrane integrated packed-bed reactor with microchannel heat exchangers. The inlet stream for the system was selected as CO_2-rich syngas. For methanol synthesis to produce DME and hydrogenation reactions, Cu-ZnO/Al_2O_3 and HZSM-5 catalysts were preferred. The cooling stream in the microchannel heat exchanger systems was reported as H_2 to enhance catalytic performance of the reactions. Temperature variation through the packed-bed reactors were oscillated from 523K to near 543K with an approximate difference of 20°C. In addition, the effect of number of the packed-bed reactors on performance metrics were studied thoroughly. It was reported that number of packed-bed reactors were calculated as twelve reactors. While the CO, CO_2 conversions and DME yield were rising significantly with the increasing number of the reactors, pressure drop increased steadily. Furthermore, the effect of the inlet velocity

was investigated. Flow rate of converted CO_2 amount per catalyst weight reduced with the rising inlet velocity, due to the lower contact time between the catalyst and the reactants. On the contrary, the flow rate of converted CO_2 amount per reactor volume (m^3) was affected positively with the increasing inlet velocities. It was reported that superior contact area between the heat exchanger streams and the membrane layer in contrast with commercial packed-bed reactors allowed to achieve results of 58.9% CO conversion, 71.5 CO_2 conversion and 56.9% DME yield.

2.3. Steam Selective Membranes

Wang *et al.* [47] investigated a novel method based on 2-step hydrothermal synthesis of SOD membrane. Among hydrophilic zeolite membranes, LTA was one of the major membrane. In this study it was aimed to synthesize SOD membrane by a novel method and contrasting the results in terms of permeability values with LTA membrane as a base case scenario. The studied permselectivities were H_2O/ H_2 , H_2O/CH_4 and H_2O/CO_2. The sets of experiments were made at a temperature range of 125-250°C and at atmospheric pressure. At 125 °C, H_2O permeability of the SOD membrane was reported 6 x 10^{-8} mol m^{-2} s^{-1} Pa^{-1} at the beginning of the 50 h test. Towards the end of the test, the permeability values of the SOD membrane started to oscillate and finalized as almost 7 x 10^{-8} mol m^{-2} s^{-1} Pa^{-1}. At 250°C, SOD membrane demonstrated a H_2O permeability of near 6.5 x 10^{-8} mol m^{-2} s^{-1} Pa^{-1}. In addition to the H_2O permeance tests, permselectivities were also calculated against elevating temperature. While at 125°C, permselectivity of H_2O/CO_2 was reported around 31.4, at 250°C it was reduced to 22.6. It was observed that the permselectivity values were negatively affected by the increasing temperature (Table 2.9).

Table 2.9. Experimental data of the permselectivities.

	125°C	**150°C**	**175°C**	**200°C**
H_2O/ H_2	8.1	6.7	5.2	4.6
H_2O/CH_4	17.9	16.4	15.3	14.5
H_2O/CO_2	31.4	28.4	25.2	22.6

Raso *et al.* [49] investigated $H_2O/H_2/CO_2$ separation performances for different zeolite membranes. Zeolite membranes which are selected for comparison in terms of their permeability values at a temperature range of 160 to 260°C were mordenite, membrane T, LTA and chabazite X. It was observed that at 160°C hydrophilic mordenite membrane had a separation factor for H_2O/CO_2 and H_2O/H_2 both around 2. With the increasing temperature the separation performances of either H_2O/CO_2 and H_2O/H_2 were decreased to nearly 1.5. Membrane T achieved much more successful separation performance than mordenite membrane. It was observed that permselectivity values of H_2O/CO_2 and H_2O/H_2 were nearly 15 and 30, respectively at 160°C. Through higher temperatures the permselectivities values decreased. Permselectivity of H_2O/CO_2 affected the most from this temperature increase, it was decreased to nearly 1 from 30 while H_2O/CO_2 value decreased to around 5 from 15. Thus, despite higher permselectivity performance of the membrane, it drastically affected from the temperature increase. LTA membrane had the highest separation performance among the investigated membranes. Permselectivity values of H_2O/CO_2 and H_2O/H_2 were 300 and 70, respectively at 160°C. On the other hand, it had also negatively affected from the temperature elevation and the performances dropped nearly 20 and 6, respectively at 260°C. Chabazite X demonstrated an average separating performance in contrast with other studied membranes. Between the operating temperatures the H_2O/CO_2 values were oscillated at the intervals of 1 and 10.

3. MATHEMATICAL MODELING

3.1. Description of the Multifunctional Reactor

Schematic illustration of the membrane integrated microchannel reactor is presented in Figure 1. A unit cell of the multifunctional reactor consists of reaction and permeate channels separated by a steam selective membrane. The unit cells are repeating along the multichannel reactor as shown in Figure 1. The channels are considered to have rectangular geometry considering their relative ease of micromachining with high precision [50] and compatibility with the mathematical models constructed previously in our group. Reaction and permeate channels are designed identically with dimensions of 3 x 10^{-4} m (*H*), 6 x 10^{-4} m (*W*) and 1.5 x 10^{-1} m (*L*). Sizing of the channels are based on the trade-off between pressure-drop and transport coefficients [50]. Reaction channel is where the catalytic activities occur between the porous media and the reactants. A catalyst layer of 5 x 10^{-5} m is immobilized into the reaction channels positioning on the *x*-*z* plane. CuO/ZnO/Al_2O_3 (CZA) catalyst is selected for the reaction due to the it's high catalytic performance and great thermal stability to avoid deactivation problem [6, 8, 51].

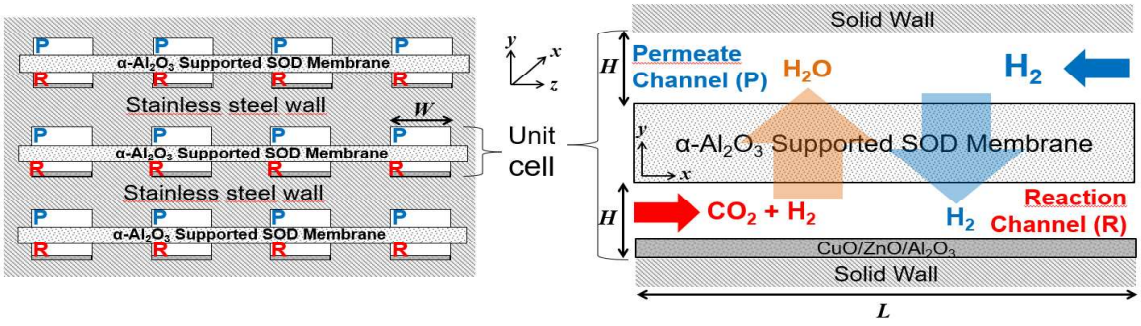

Figure 3.1. Schematic illustration of the multichannel reactor (left) and the unit cell (right).

To physically separate H_2O from the reaction channel for enhancing reactor performance, an α-Al_2O_3 supported SOD membrane is used. The *in-situ* separation of by-product H_2O leads to boost in forward reaction kinetics according to Le Chatelier's principle. The membrane layer has 1 x 10^{-3} m of thickness in the microchannel reactor. Hydrogen is used as the sweep gas in the permeate channel in order to carry out the separated steam from the reaction channel and to

enrich the feed stream due to the H_2 permselectivity of the membrane. In other words, the membrane can also promote CO_2 hydrogenation by permeating H_2 from the permeate to reaction channel.

Reactor is operated under co-current flow configuration while both reaction and permeate channel runs at the same temperature and pressure. Recent studies pointed out negligible differences in the reactor performance upon setting a pressure gradient between the inlets of reaction and permeate channels [45, 52]. In this regard, reactive mixture and sweep streams are always fed at identical pressures. From a practical point of view, this setting prevents operational complexities due to regulation of different inlet pressures. The microchannel system is studied under isothermal conditions at 523 K. This temperature is selected considering endothermic nature of the reaction and experimental data which was obtained from the literature for the kinetic investigation of the study [16, 53]. The multifunctional reactor is operated at 15 bar and with a H_2:CO_2 ratio of 3 as default operating parameters. W/F_{CO_2} is fixed at 40 g_{cat} h mol^{-1}, due to this constant ratio, for each set of pressure inlet flow rate of CO_2 is varied in different ranges. This circumstance originates from concentration change of the inlet reaction components with the increasing pressure. Inlet linear velocity is calculated as 9.4 x 10^{-3} m s^{-1} for the default case, which ensures sufficient contact opportunity between the catalyst layer and reactants [54, 55].

To examine the effects of membrane assisted operation on chosen performance metrics, namely CO_2 conversion, CO_2 converted and syngas composition (defined in Equations 3.1-3.3, respectively); the impact of inlet pressure, inlet H_2:CO_2 ratio, flow configuration, inlet reaction and permeate channel velocities are investigated. Plan of the parametric study is presented in Table 3.1. At 523 K, H_2:CO_2 = 3 and the specified pressure (5–15 bar), permeate channel inlet velocity is set to 1, 2, 4 and 6 times the pertinent reaction channel inlet velocity ($v^{p}_{rxn,c}$) which is changed by adjusting the residence time ($W/F_{CO_2,in}$) accordingly as given in Table 3.1. In all cases, catalyst layer dimensions and the mass of catalyst coated to one reaction channel (W), calculated by using the physical properties of the $CuO/ZnO/Al_2O_3$ catalyst presented in Section 3.2, remain constant. Default values of the reaction channel inlet linear velocities at 5, 10 and 15 bar (2.8, 1.4 and 0.94×10^{-2} m s^{-1}, respectively) are based on the residence time of 40 g_c h mol^{-1} and computed by using the ideal gas equation of state. It is assumed that reactive mixture

(H_2 +CO_2) and sweep (H_2) streams are distributed uniformly to each channel. This assumption is based on the uniformity of channel dimensions and the thickness of the catalyst layer along the channel, both of which can be achieved by the catalyst coating and precise micro–manufacturing techniques [56]. Performance metrics are quantified as

$$CO_2\ conversion = \frac{F_{CO_2,in} - F_{CO_2,out}}{F_{CO_2,in}}\ x\ 100\ , \tag{3.1}$$

$$Converted\ CO_2\ amount =\ F_{CO_2,in}\ x\ CO_2\ Conversion(\%)\ , \tag{3.2}$$

$$Syngas\ composition\ = \frac{n_{H_2} - n_{CO_2}}{n_{CO} + n_{CO_2}}. \tag{3.3}$$

Table 3.1. Default values and ranges (presented as boldface) of the operating parameters.

Parameter	**Default Value / Setting**		**Range**	
Temperature (K)	523		–	
Residence time, $W/F_{CO_2,in}$) (g_c h mol^{-1})	40		**40–320** (40, 80, 160, 320) (at 5 and 10 bar) **5–320** (5, 6.7, 10, 20, 40, 80, 160, 320) (at 15 bar)	
Pressure (bar)	15		**5–15** (5, 10, 15)	
Molar inlet H_2:CO_2 ratio (–)	3		**2–4** (2, 3, 4)	
Flow direction	Co–current		Co/counter–current	
Reaction channel inlet velocity, $v^p_{rxn,c}$ ($\times 10^2$ m s^{-1})	5 bar	2.8	5 bar	**3.5×10^{-1}–2.8** ($v^5_{rxn,1}$=3.5×10^{-1} ; $v^5_{rxn,2}$=7×10^{-1}, $v^5_{rxn,3}$=1.4; $v^5_{rxn,4}$=2.8)
	10 bar	1.4	10 bar	**1.75×10^{-1}–1.4** ($v^{10}_{rxn,1}$=1.75×10^{-1}, $v^{10}_{rxn,2}$=3.5×10^{-1}, $v^{10}_{rxn,3}$= 7×10^{-1}, $v^{10}_{rxn,4}$=1.4)
	15 bar	0.94	15 bar	**1.18×10^{-1}–7.5** ($v^{15}_{rxn,1}$=1.18×10^{-1}, $v^{15}_{rxn,2}$=2.35×10^{-1}, $v^{15}_{rxn,3}$=4.7×10^{-1}, $v^{15}_{rxn,4}$=9.4×10^{-1}, $v^{15}_{rxn,5}$=1.9, $v^{15}_{rxn,6}$=3.8, $v^{15}_{rxn,7}$=5.6, $v^{15}_{rxn,8}$=7.5)
Permeate channel inlet velocity ($\times 10^2$ m s^{-1})	5 bar	2.8	5 bar	$v^5_{rxn,c}$, $2v^5_{rxn,c}$, $4v^5_{rxn,c}$, $6v^5_{rxn,c}$ (c = 1, 2, 3, 4)
	10 bar	1.4	10 bar	$v^{10}_{rxn,c}$, $2v^{10}_{rxn,c}$, $4v^{10}_{rxn,c}$, $6v^{10}_{rxn,c}$ (c = 1, 2, 3, 4)
	15 bar	0.94	15 bar	$v^{15}_{rxn,c}$, $2v^{15}_{rxn,c}$, $4v^{15}_{rxn,c}$, $6v^{15}_{rxn,c}$ (c = 1, 2, 3, 4); $6v^{15}_{rxn,c}$ (c = 5, 6, 7, 8)

3.2. Reaction Network and the Kinetic Model

In order to catalyze the conversion of relatively more stable CO_2 into reactive CO *via* hydrogenation reaction $CuO/ZnO/Al_2O_3$ catalyst is used. As mentioned in Section 3.1, a $5x10^{-5}$ m thick catalyst layer is washcoated to the inner wall of the reaction channel. Homogeneous gas-phase reactions are neglected due to their slower reaction kinetics in contrast with the reactions which are taking place between the surface of the porous medium and reactant fluid [59]. To inhibit undesired methanation reaction with other side reactions and catalyst deactivation as a consequence of Cu agglomeration, the temperature is limited to 523 K [58]. Reaction kinetics adopted from the literature is presented below [16] as

$$r_{RWGS} = k_0\, e^{-(\frac{E_a}{R\,T(K)})} \left[y_{CO_2} y_{H_2} - \frac{y_{CO}\; y_{H_2O}}{K_{eq}} \right] C_{FP}. \tag{3.4}$$

In order to quantify the reaction rate, reaction parameters are given in Table 3.2.

Table 3.2. Reaction parameters.

Parameter	Value	Unit
k_0	2.1852 x 10^5	mol kg_{cat}^{-1} s^{-1}
E_a	7.1623 x 10^4	J mol^{-1}

Even though the reaction rate is not being majorly affected from the reactor pressure due to its equimolar nature, it is observed that with the increasing pressure some deviations occurs in the reaction rate. To avoid these deviations up to 30 bar, a pressure correction factor is generated in the same work where the reaction kinetics are adopted. Pressure correction factor is introduced as

$$C_{FP} = \frac{P(Pa)}{1\;x\;10^5}^{(0.5-\frac{P(Pa)}{250\;x\;10^5})}. \tag{3.5}$$

For computation of reaction kinetics, equilibrium constant of the reaction can be determined *via* using Gibbs free energy by

$$K_{eq} = \exp\left(-\frac{\Delta G_{rxn}}{R\,T}\right), \tag{3.6}$$

where Gibbs free energy is formulated in Equations 3.7-3.10 and the related constants are presented in Table 3.3. Gibbs free energy is quantified by

$$G_{rxn} = \sum_{i=products} n_i G_{f,i} - \sum_{i=reactants} n_i G_{f,i}\,, \tag{3.7}$$

$$\frac{G_{f,i}}{R\,T} = \frac{H_{f,i}}{R\,T} - \frac{S_{f,i}}{R\,T}, \tag{3.8}$$

$$\frac{H_{f,i}}{R\,T} = a_1 + a_2\frac{T}{2} + a_3\frac{T^2}{3} + a_4\frac{T^3}{4} + a_5\frac{T^4}{5} + \frac{b_1}{T}, \tag{3.9}$$

$$\frac{S_{f,i}}{R\,T} = a_1 \ln T + a_2 T + a_3\frac{T^2}{2} + a_4\frac{T^3}{3} + a_5\frac{T^4}{4} + b_2. \tag{3.10}$$

Table 3.3.Gibbs free energy coefficients [59].

Species	a_1	a_2(x 10^3)	a_3(x 10^6)	a_4(x 10^9)	a_5(x 10^{12})	b_1(x 10^{-4})	b_2
CO	3.58	-0.61	1.02	0.91	-0.90	-1.43	3.51
H_2	2.34	7.98	-19.5	20.2	-7.38	-0.092	0.68
CO_2	2.36	8.98	-7.12	2.46	-0.14	-4.84	9.90
H_2O	4.20	-2.04	6.52	-5.49	1.77	-3.03	-0.85

Physical properties of the CZA catalyst are adopted from the literature and presented in Table 3.4.

Table 3.4. Properties of CZA catalyst [16, 54].

Properties	Values	Unit
Solid density of the catalyst	5904	kg m^{-3}
Porosity	0.55	-
Tortuosity	1.64	-
Thermal conductivity	24.2	W m^{-1} K^{-1}

To validate the microchannel reactor, the proposed model is compared with the experimental data obtained from [60] in terms of CO_2 conversion with respect to catalyst weight per inlet volumetric flow rate of CO_2. After the contrast between the model and the experimental data which is explained thoroughly in Section 4.1, W/F_{CO_2} ratio is found to be eligible to be fixed at $W/F_{CO_2} = 40$ g_{cat} h mol^{-1} for further investigations in this study.

3.3. Membrane Model

Combining the benefits of the microchannel reactor with a steam selective membrane enhances reactor performance *via in-situ* separation of H_2O from the reaction channel and dosing H_2 into the reaction channel offers a significant potential for relaxing thermodynamic limitations of the RWGS reaction. In order to integrate the hydrophilic membrane into the microreactor system, the approach of Ji *et al.* [61] is adopted; this adoption is formulated by Koybasi *et al.* [45, 52] previously in our group and customized to RWGS in the current study. In the context of this methodology, membrane layer is represented as a zero-thickness wall between the both reaction and permeate channels. In addition, source terms are assigned to the neighboring mesh cells to the membrane layer towards channels. Due to the discontinuity between the fluid flows originated by the wall, Navier-Stokes equations cannot be used to quantify the mass transfer throughout the membrane. This complication is overcome by merging a user defined function (UDF) into the ANSYS (v.19.2) platform used for simulating he proposed reactor as described in Section 3.4. The implemented UDF performs the computation of the source terms (in kg m^{-3} s^{-1}) which are adjacent mesh cells to the membrane both in reaction and permeate channel and represented by sink and source zones, respectively. An illustration of the membrane model is presented in Figure 3.2. Furthermore, computation of

the source terms is based on Fick's Law [61] which states that the mass flux through the channels is a function of the partial pressure differences between the components in the reaction and permeate channels, and the permeability of the membrane. The mass transfer through membrane is quantified as

$$J_i = Perm_i \left(P_{i,reaction} - P_{i,permeate}\right). \tag{3.11}$$

Cross-membrane mass flux is generated in units of mol m^{-2} s^{-1}. On the other hand, source terms are created in unit of kg m^{-3} s^{-1}. Thus to provide the units needed, molecular weights of the components and length of a mesh cell edge are needed to be considered. Source terms are calculated by the UDF as

$$S_i = \frac{J_i \, M_i}{L_{edge}}. \tag{3.12}$$

After the computation of source terms by integrated UDF, the values are stored using user defined memory (UDM). The created UDM values on the sink zone are multiplied by -1 to represent source zone values across the membrane which are mentioned as neighboring mesh cells to the zero-thickness wall.

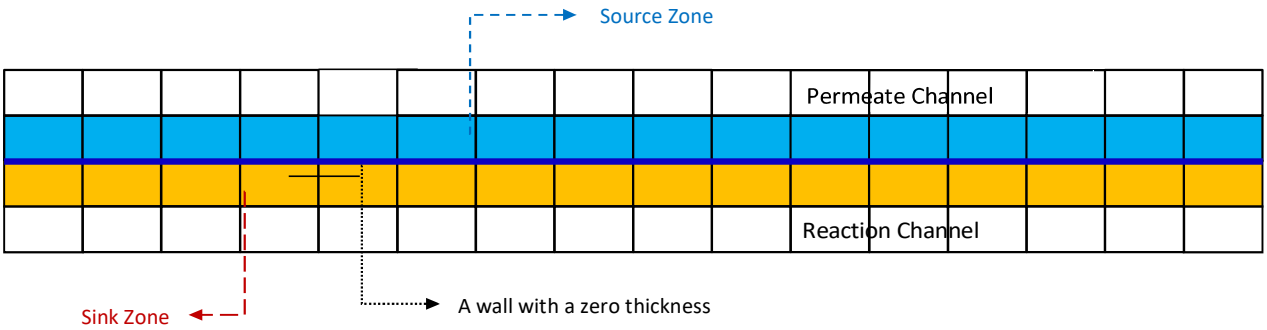

Figure 3.2. Illustration of membrane model.

Several membranes which show a significant H_2O separation performance are reported in the study of Li *et al.* [14] as SOD, ZSM-5, MOR, LTA, FAU and Zeolite-T. Membrane material must be considered according to the expected performance of H_2O permeance and permselectivity of H_2O against other components (CO_2, H_2, CO). In addition to these expectations, as previously mentioned, H_2 is used as the sweep gas in the permeate channel to enhance reactor performance. Thus, the selected membrane must allow H_2 permeance in a certain level to fulfill these requirements. Taking all these considerations into account, SOD membrane is determined as one of the top satisfactory materials for the multifunctional reactor operation. At 473 K, H_2O permeability and steam-H_2 permselectivity (S_{H_2O/H_2}) values are reported as 6.8 x 10^{-8} mol m^{-2} s^{-1} Pa^{-1} and 4.6 [12, 62]. In addition, the high surface area to volume ratio ($\geq 10^4$ m^2 m^{-3}) of microchannel reactors allows decoration of higher membrane surface areas per unit volume [64]. The reported data for the membrane properties are not available at temperatures higher than 473 K, so for the operating temperature of our system (523 K) the H_2O permeability value is selected 3 x 10^{-8} mol m^{-2} s^{-1} Pa^{-1}, this assumption is made considering the appearance of competitive adsorption which hinders the permeance capability [62, 65]. In this study, only mass transfers of H_2 and H_2O are permitted through the membrane while transfer of other components are neglected.

3.4. Solution Methodology and Associated Equations

Mathematical modeling of the membrane-integrated microchannel reactor (Fig. 3.1) involves formulation of the mass and momentum transports under isothermal operation. It is comprehensively investigated and confirmed in the previous study's that there are no significant differences between the results of 2-D and 3-D models, consequently to save computational cost the microchannel system is selected to be modeled in 2-D along the *y*-*z* axis [52, 65]. Furthermore, to observe the temperature change through the microreactor system and to verify the isothermal assumption, the reactor is also tested for the so-called adiabatic operation involving convective heat transfer between gas phases, porous zone and inter-channel heat transfer in Section 4.2. In this case, heat loss across the walls are nullified. Due to reaction kinetics of gas-phase homogeneous reactions are relatively slower than reactions which occurs between solid and gas phases, they are neglected and the reaction is only appear in the porous zone of the microreactor [57]. In order to run simulations under ANSYS (v.19.2) platform, linear velocity, temperature and H_2:CO_2 ratio are defined to system as inlet; on the other hand,

pressure is entered as outlet [55]. The boundary conditions of the microreactor are illustrated in Figure 3.4.

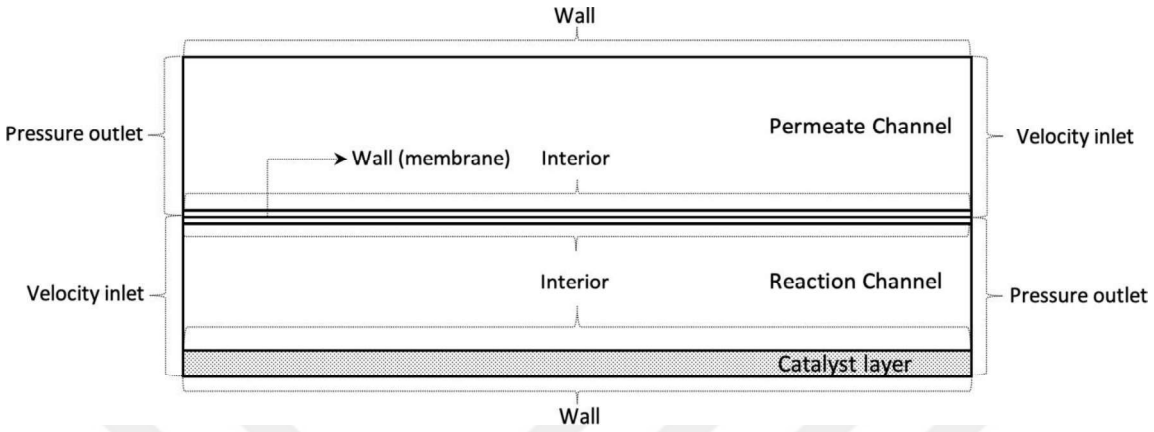

Figure 3.3. Representation of microchannel reactor boundary conditions.

A discontinuity in the mathematical model is showed between the flows of both channels originated from the assumption of zero thickness wall in the membrane model. On the contrary of the membrane model, the flow in the porous zone shows a continuous characteristic between the solid-gas interphase [45]. To describe the reactor model, related equations are presented in Table 3.5. For the adiabatic study, Equations 3.17-3.19 are included in Table 3.5. It is worth noting that the model equations in Table 3.5 are presented in their generalized form. However, in the current simulations, flow in both channels is assumed to be incompressible and the fluids follow the Newtonian behavior. Incompressibility is justified by the negligible pressure drop in the microchannels, which is reported in the literature for the similar combinations of reactor geometry and operating conditions [66].

In order to perform simulations under ANSYS (v.19.2) platform, finest reactor geometry is constructed via Gambit software (v. 2.3.16). The microreactor is formed of 5.76×10^5 square mesh cells, each with an edge length of 1.25×10^{-5} m. The multifunctional reactor model consists of three major parts which are membrane functioning area, reaction and permeate channels. Reaction and permeate channels are identical in geometry and consist of 2.76×10^5 cells each. Membrane functioning area contains sink and source zones, which are also identical in geometry and both consists of 1.2×10^4 cells. In order to quantify physical properties of the gas mixture such as viscosity, molecular weight and diffusivities a set of correlations can be

found in the literature [68]. These correlations are integrated into the ANSYS platform for microreactor simulations *via* UDFs. In addition to these correlations, kinetic model (Section 3.2) and membrane model (Section 3.3) are also integrated *via* UDFs.

Table 3.5. Model equations regarding multifunctional reactor (FP: Fluid phase, PZ: Porous Zone, ML: Membrane Layer).

Continuity eq.	$\nabla.(\rho_m \vec{\boldsymbol{v}}) = 0$	(3.13)
Momentum equation (FP)	$\nabla.(\rho_m \vec{\boldsymbol{v}}\vec{\boldsymbol{v}}) = \nabla p + \nabla.\left[\mu_m\left(\nabla\vec{\boldsymbol{v}} + (\nabla\vec{\boldsymbol{v}})^T - \frac{2}{3}(\nabla.\vec{\boldsymbol{v}})I\right)\right]$	(3.14)
Momentum equation (PZ)	$\nabla.(\rho_m \vec{\boldsymbol{v}}\vec{\boldsymbol{v}}) = \vec{\boldsymbol{F}} - \nabla p + \nabla.\left[\mu_m\left(\nabla\vec{\boldsymbol{v}} + (\nabla\vec{\boldsymbol{v}})^T - \frac{2}{3}(\nabla.\vec{\boldsymbol{v}})I\right)\right]$ $\vec{\boldsymbol{F}} = -\left(\frac{\mu_m}{\alpha}\vec{v} + \frac{C_2}{2}\rho_m\lvert\vec{v}\rvert\vec{v}\right); \alpha = \frac{d_p^2}{150}\frac{\varepsilon_{cat}^3}{(1-\varepsilon_{cat})^2};\ C_2 = \frac{3.5}{d_p}\frac{(1-\varepsilon_{cat})}{\varepsilon_{cat}^3}$	(3.15)
Species mass equation (FP)	$\nabla.(\rho_m \vec{v} Y_i) = -\nabla.\vec{J_i};\ \vec{J_i} = -\rho_m D_{i,m}\nabla Y_i$	(3.16)
Energy equation (FP)	$\nabla.\left(\rho_m\ c_{p,m}\ \vec{v}\ T\right) = \nabla.(k_m\ \nabla T)$	(3.17)
Energy equation (PZ)	$\nabla.\left(\rho_m\ c_{p,m}\ \vec{v}\ T\right) = \nabla.\left(k_{eff}\ \nabla T\right) \sum(\Delta H_{rxn} r_{rxn})$	(3.18)
Energy equation (ML)	$\nabla.(k_w\ \nabla T) = 0$	(3.19)

4. RESULTS AND DISCUSSION

Effects of inlet pressure, reaction and permeate channel velocities, H_2:CO_2 ratio and flow configuration on performance metrics (CO_2 conversion, converted CO_2 and syngas composition; Equations (3.1)-(3.3), respectively) are investigated. Moreover, the mathematical model is benchmarked against the literature-based experimental data. Furthermore, sizing of a pilot scale multichannel reactor based on green hydrogen production using 1 MW electrolyzer [68] is studied. The scaled-up reactor is assessed considering converted CO_2 amount per catalyst weight. Finally, the performance of multichannel reactor is compared with a packed-bed reactor from the literature [16] where the reaction kinetics are obtained.

4.1. Model Verification

In an attempt to verify the reactor and kinetic models, as well as the correlations used for the physical properties of the species, experimental results adopted from the literature [16] are compared with those obtained from the simulations. Comparison of the experimental data and the model outputs are presented in Figure 4.1.

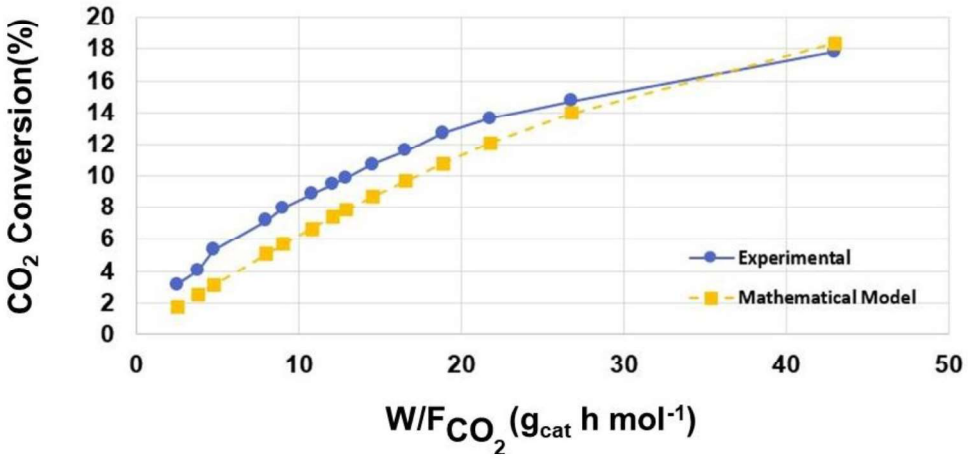

Figure 4.1. Comparison between the experimental data and the data predicted from the model (T = 523 K, P = 1 bar, H_2:CO_2 = 6).

Simulations are carried out under the same operating parameters with the experimental work in the literature [16] which is carried out at 250°C, atmospheric pressure, and inlet H_2:CO_2=6. The experimental work does not involve membrane integration. Therefore, membrane mass transfer is deactivated in the simulations and the system operated as membraneless reactor. As mentioned in Section 3.2, W/F_{CO_2} ratio is considered as the parameters for calculating the linear flow rates of inlet streams. After the comparison between the experimental data and the simulation results at various W/F_{CO_2} ratios , the ratio of 40 g_{cat}^{-1} h mol^{-1} is selected where the model satisfactorily predicts the experimental data. At $W/F_{CO_2} =$ 40 g_{cat} h mol^{-1}, the mathematical model calculated CO_2 conversion as 17.8%. Despite experimental data unavailable at exact $W/F_{CO_2} = 40$ g_{cat} h mol^{-1} point in Figure 4.1., the missing data is calculated via linear regression and 17.3% CO_2 conversion is obtained. In addition, combining the kinetic model with thermodynamic relations and actuated assumptions the reactor model carries the characteristics and shows the capability of predicting the outcomes of an actual system.

4.2. Validation of Isothermal Conditions

Near-isothermal conditions assumption is made for the microchannel reactor. This assumption is tested and presented in Figure 4.2. For this purpose, energy conservation equations, presented in Table 3.1, are solved along with the mass and momentum conservation equations in ANSYS platform. Temperature change along the reactor is investigated for both co and counter-current flow configurations. Co-current flow configuration demonstrates a steady decline in temperature starting from 523 K and at the end of the reactor outlet temperature is observed as 516 K. On the other hand, counter-current flow configuration shows a minimum due to the endothermic nature of the reaction, followed by equilibration at 523 K, the inlet temperature of the sweep gas. The temperature change observed for both configurations is similar. While co-current flow showed 1.3% change from beginning of the reactor to end, counter-current flow exhibited 1.4% temperature change from beginning of the reactor to the left-mid region. Considering these results, near-isothermal conditions assumption is found suitable to be applied and in order to save computational power energy conservation equations are disabled for simulations.

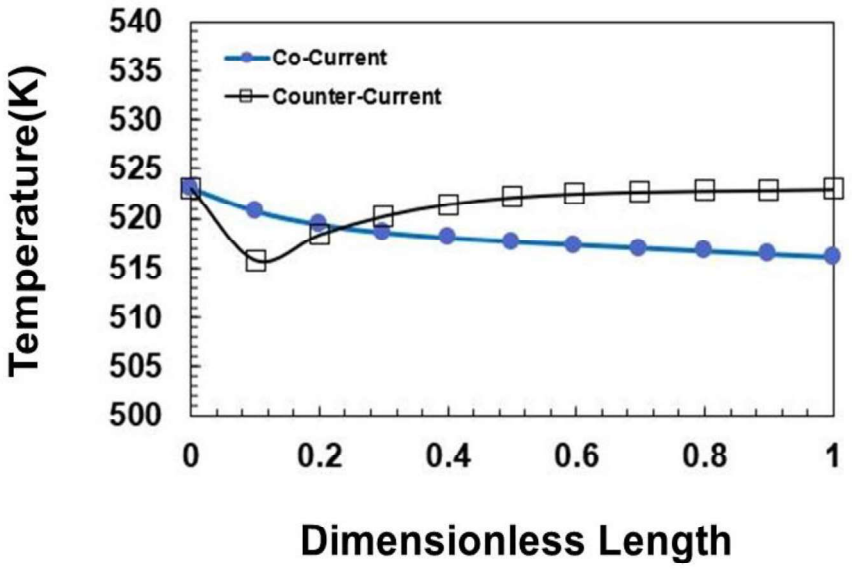

Figure 4.2. Temperature change along the reactor in co and counter-current flow configurations (T = 523 K, P = 5 bar, H_2:CO_2 = 3).

4.3. Effects of Reactor Pressure, Reaction and Permeate Channel Inlet Velocities on CO_2 Conversion and the Amount of CO_2 Converted

The effects of the velocities of the reactive mixture (H_2 + CO_2) and sweep (H_2) streams on the reactor performance are investigated at 523 K, H_2:CO_2 = 3, and pressures of 5, 10 and 15 bar. Combinations of the reactive mixture and sweep gas inlet velocities are presented in Table 3.1. For example, at 5 bar, each reaction channel inlet velocity value ($v^5_{rxn,c}$) is coupled with permeate channel inlet velocities set to $v^5_{rxn,c}$, $2v^5_{rxn,c}$, $4v^5_{rxn,c}$ and $6v^5_{rxn,c}$ (please refer to Section 3.1 for the definition and formulation of inlet velocities). The results, expressed in terms of per cent CO_2 conversion and moles of CO_2 converted defined in Equations (3.1) and (3.2); respectively. For benchmarking purposes, these metrics are computed also for the membraneless case (labeled as "NM"). The results are presented in Figures 4.3 and 4.4 for 5 bar, 4.5 and 4.6 for 10 bar and 4.7 and 4.8 for 15 bar operation. At 5 bar, the increase in reaction channel inlet velocity had a negligible impact on CO_2 conversion in membraneless case (Figure 4.3). The integration of steam selective membrane to the microchannel reactor enhances the reactor performance and increases CO_2 conversion from 15.6% to 32.0%. The increment in the reaction channel inlet velocity affects the CO_2 conversion negatively, this circumstance is a result of decrease of the residence time between the catalyst and the feed stream. Residence

time and reaction channel inlet velocity are inversely proportional, thus increase in the reaction velocity reduces reactor performance. H_2 is used as bifunctionally in permeate channel to sweep the unwanted product H_2O and to enhance the reactor performance *via* its *in-situ* transport into the reaction channel. So, inlet permeate channel velocity has a positive impact on the performance metric. CO_2 conversion rises from 32.0% to 42.1% with the elevation of the permeate velocity. This performance increase can be explained with the increase of H_2 concentration in permeate channel with the greater permeate velocity. Thus, the concentration of by-product H_2O decreases in the channel and correspondingly the extent of H_2O transfer from reaction to permeate channel increases.

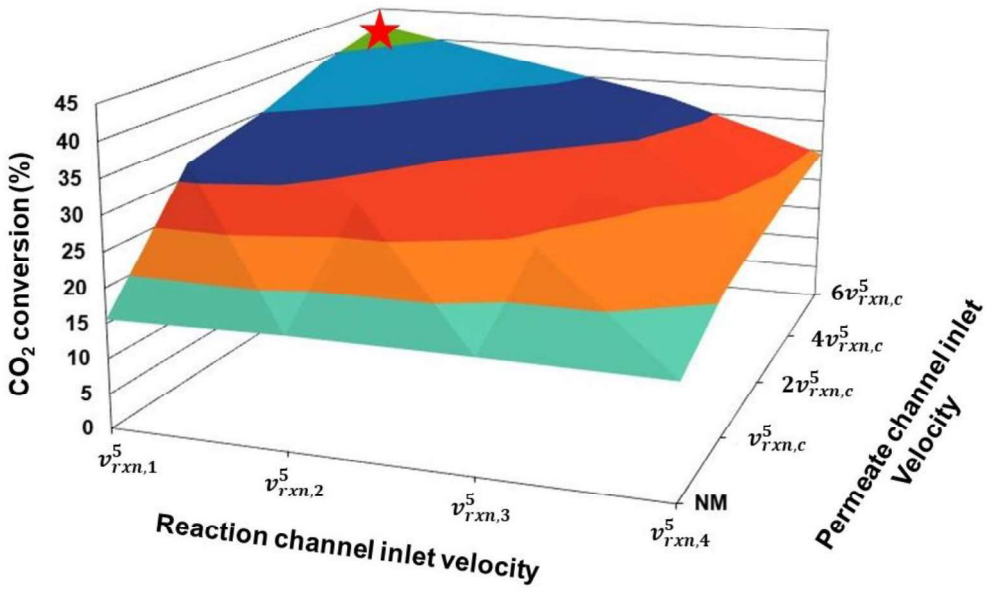

Figure 4.3. Effect of reaction and permeate channel inlet velocities on CO_2 conversion at 5 bar (T = 523 K, H_2:CO_2 = 3, flow direction in membrane–integrated cases: co–current).

The membrane mass transfer occurs regarding Fick's Law as previously mentioned in Section 3.3. Thus the mass transfer through membrane is correlated with the partial pressure differences of the components between the channels. Consequently, the best performance in terms of CO_2 conversion is obtained at reaction velocity $v^5_{rxn,1}$ and permeate velocity $6v^5_{rxn,1}$ as 42.1% . In contrast with the membraneless scenario the performance metric is folded almost 3 times. The membraneless case can also be considered as the thermodynamic limit, as the reverse reaction effect is considered in the kinetic model adopted in this study (Section 3.2).

As can be seen in Figure 4.4. converted CO_2 amount demonstrates the opposite of the trend observed in the case of CO_2 conversion. The converted CO_2 amount rises considerably with increasing reaction channel inlet velocity. This outcome is a result of capacity increase in the (*i.e.*, feeding more reactant to the) reaction channel $v_{rxn,4}^5$, molar flow rate increase dominates the converted CO_2 amount. Also, the integration of the hydrophilic membrane to the microreactor positively affected the performance metric indirectly due to the improvement in CO_2 conversion. Furthermore, it is observed that with the increasing permeate channel velocity the converted CO_2 amount also increases. The best performance is noted as converted CO_2 amount folded almost 2.7 times at reaction velocity $v_{rxn,1}^5$and permeate velocity $6v_{rxn,1}^5$. In terms of capacity increase, the highest converted CO_2 amount achieved at $v_{rxn,4}^5$ and $6v_{rxn,1}^5$ respectively as 3.5 x 10^{-8} mol s^{-1}.

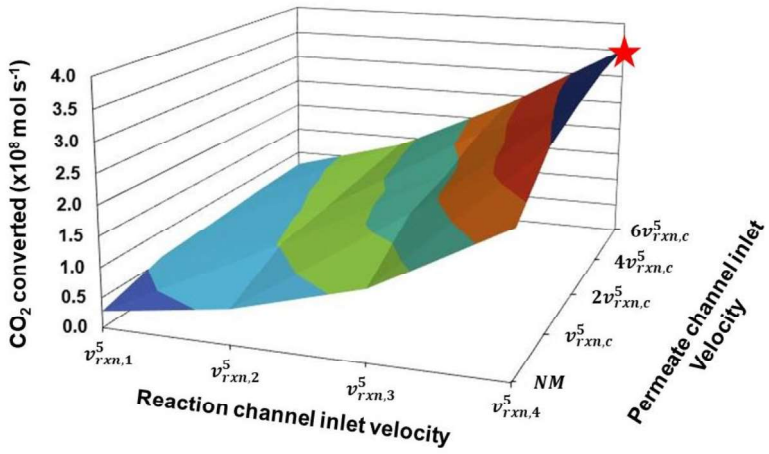

Figure 4.4. Effect of reaction and permeate channel inlet velocities on converted CO_2 amount at 5 bar (T = 523 K, H_2:CO_2 = 3, flow direction in membrane–integrated cases: co–current).

Increase in the operating pressure had a minor effect on CO_2 conversion in the absence of steam selective membrane due to equimolar stoichiometry of the reaction. Unlike with the results of the 5 bar study, the highest CO_2 conversion is achieved at reaction channel inlet velocity of $v_{rxn,1}^{10}$ as 16.3%. Only integrating hydrophilic membrane to the microchannel reactor with the same inlet velocity of reaction channel boosted the conversion to 34.3%. Thus, in contrast with 5 bar results it is observed that pressure increase had a positive impact. Even though the reaction has equimolar stoichiometry, the pressure increase affected the membrane performance and indirectly improved the CO_2 conversion. In addition, it is noted magnifying

the permeate channel inlet velocity has a major impact on reactor performance. The increase of the permeate velocity from $v_{rxn,1}^{10}$ to $6v_{rxn,1}^{10}$ escalates CO_2 conversion to 47.6%. Thus, membrane integration to the microreactor system significantly improves the CO_2 conversion which increases from 16.3% to 47.6%.

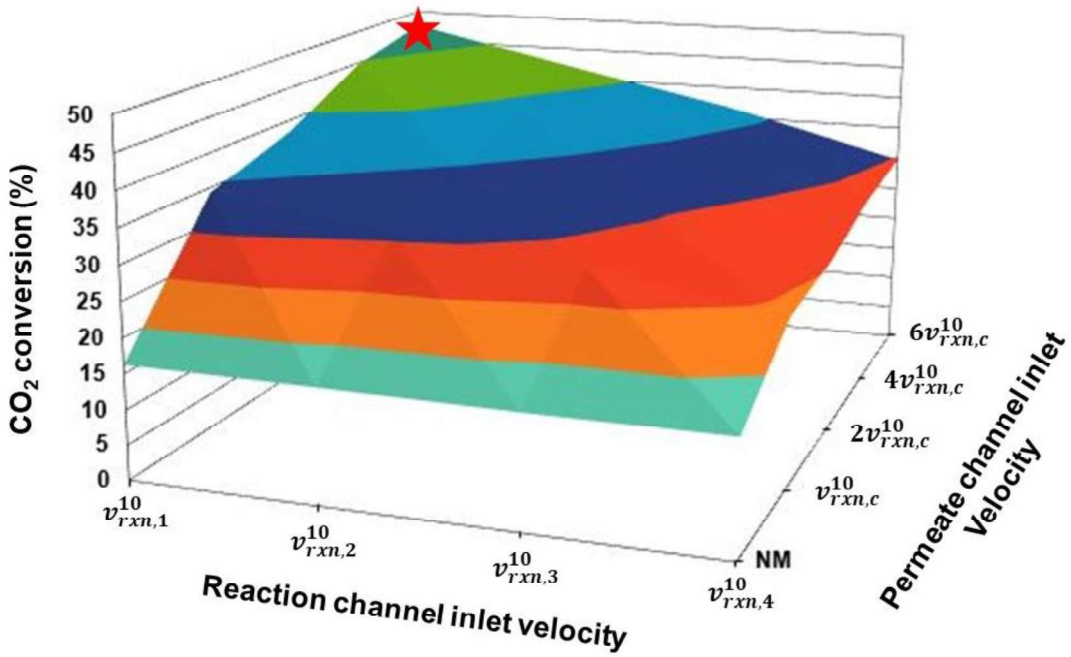

Figure 4.5. Effect of reaction and permeate channel inlet velocities on CO_2 conversion at 10 bar (T = 523 K, H_2:CO_2 = 3, flow direction in membrane–integrated cases: co–current)..

As directly proportional with the results of the CO_2 conversion at 10 bar, converted CO_2 amount is elevated in contrast with the 5 bar outcomes. The increase in the pressure affected the performance metric positively. On the contrary of the CO_2 conversion trends, reaction channel inlet velocity has a significant impact on the converted CO_2 amount due to its relation with the capacity of the component mass transfer. During the absence of the steam selective membrane, converted CO_2 increases by ~8 times, from 2.9 x 10^{-9} mol s^{-1} to 2.3 x 10^{-8} mol s^{-1}. Despite the decrease in the CO_2 conversion with the increasing inlet flow rate, converted CO_2 amount is dominated by the increment of the reaction channel inlet velocity as the flow rate is increased 8 times. Thus, this improvement in the performance metric in microchannel reactor without integration of hydrophilic membrane is rooted from the given conditions. As a consequence of its contribution to the CO_2 conversion, permeate channel inlet velocity positively affected the performance metric. At the inlet reaction and permeate channel velocities

of $v_{rxn,4}^{10}$ and $6v_{rxn,4}^{10}$,respectively, the membrane integrated microreactor demonstrates the highest converted CO_2 amount as 4.3 x 10^{-8} mol s^{-1}, which is 14% higher than the 5 bar results.

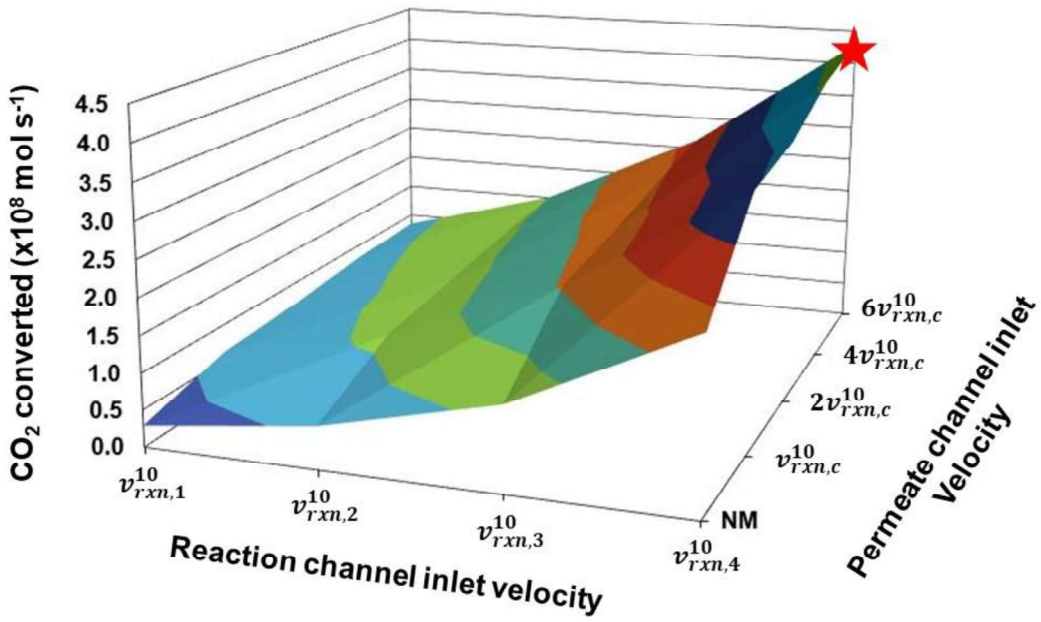

Figure 4.6. Effect of reaction and permeate channel inlet velocities on converted CO_2 amount at 10 bar (T = 523 K, H_2:CO_2 = 3, flow direction in membrane–integrated cases: co–current).

The effect of inlet reaction and permeate channel velocities at 15 bar is investigated thoroughly considering the produced syngas composition which are studied simultaneously. Regarding the reducing trend with higher inlet velocities observed in these investigations, in addition to the reaction channel inlet velocity range of 5 and 10 bar pressures, higher reaction channel inlet velocities of 2, 4, 6 and 8 folds of $v_{rxn,4}^{15}$ are studied. It is noted that with the increase in operating pressure the effect of the steam selective membrane on CO_2 conversion increases (Figure 4.7a). At reaction and permeate channel inlet velocities of $v_{rxn,1}^{15}$and $6v_{rxn,1}^{15}$, respectively the highest CO_2 conversion is achieved with 51.6%. Furthermore, higher inlet velocities of $v_{rxn,5}^{15}$, $v_{rxn,6}^{15}$, $v_{rxn,7}^{15}$ and $v_{rxn,8}^{15}$ which are equivalent to $2v_{rxn,4}^{15}$, $4v_{rxn,4}^{15}$, $6v_{rxn,4}^{15}$ and $8v_{rxn,4}^{15}$ are investigated in Figure 4.7b. It is noted that with the increasing inlet reaction channel velocity the performance metric is drastically decreased from 16.1% to 8.4% during the absence of hydrophilic membrane. On the other hand, at channel inlet velocities $v_{rxn,4}^{15}$ and $6v_{rxn,4}^{15}$, while with the integration of steam selective membrane 32.2% CO_2 conversion is

achieved, with the increasing inlet velocities CO_2 conversion is decreased to 8.6%. The results of this study indicate two major outcomes. Firstly, the performance metric drops excessively with higher reaction channel inlet velocities. Secondly, the effect of the steam selective membrane becomes insignificant at high permeate channel velocities. As mentioned before, the conversion in the absence of the membrane is indicated as 8.4% and the conversion reached to 8.6% with the integration of steam selective membrane.

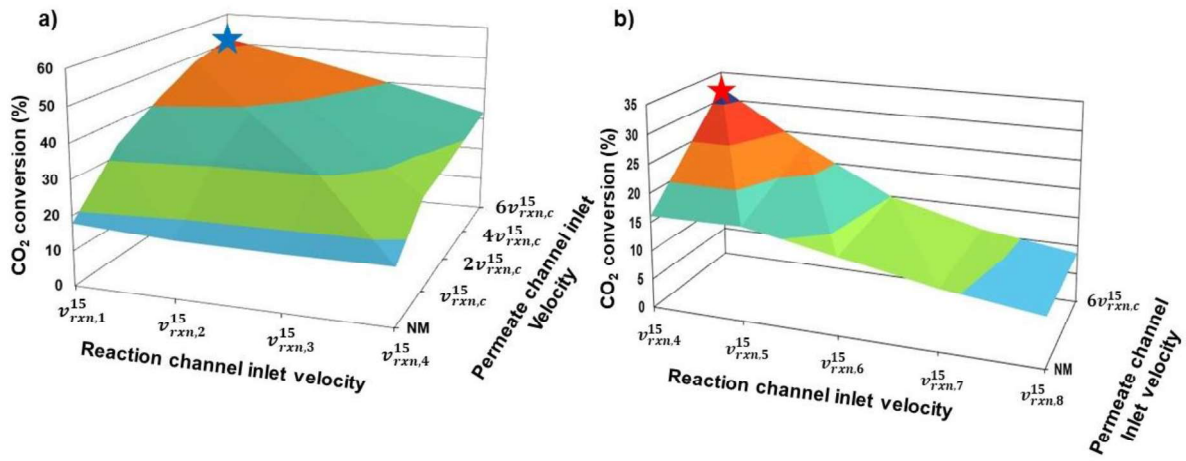

Figure 4.7. Effect of reaction and permeate channel inlet velocities on CO_2 conversion at 15 bar (T = 523 K, H_2:CO_2 = 3, flow direction in membrane–integrated cases: co–current).

Converted CO_2 reaches to the highest amount at 15 bar studies, due to the superior membrane performance at relatively higher pressure. On the contrary of CO_2 conversion, converted CO_2 amount significantly increased with higher inlet velocities and pressures (Figure 4.8). It is observed that converted CO_2 amount achieved its best performance at $v^{15}_{rxn,4}$ in the absence of the hydrophilic membrane with 2.3 x 10^{-8} mol s^{-1}. The integration of the membrane remarkably affects the microchannel system in terms of converted CO_2 amount. In order to demonstrate the impact of the steam selective membrane, at fixed operating parameters ($v^{15}_{rxn,4}$, $v^{15}_{rxn,4}$) with the integration of the membrane, converted CO_2 amount increases by 1.7 times, from 2.3 x 10^{-8} mol s^{-1} to 3.8 x 10^{-8} mol s^{-1}. It is observed that in the velocity range from $v^{15}_{rxn,1}$ to $v^{15}_{rxn,4}$ the leading converted CO_2 amount is noted as 4.7 x 10^{-8} mol s^{-1} at reaction and permeate channel inlet velocities $v^{15}_{rxn,4}$ and $6v^{15}_{rxn,4}$, respectively. As mentioned in Figure 4.7, CO_2 conversion drops drastically with the higher reaction channel inlet velocity values. At

reaction and permeate channel inlet velocities $v_{rxn,8}^{15}$ and $6v_{rxn,8}^{15}$, respectively, the multifunctional reactor reaches the best performance in terms of converted CO_2 amount with 4.7 x 10^{-8} mol s^{-1}.

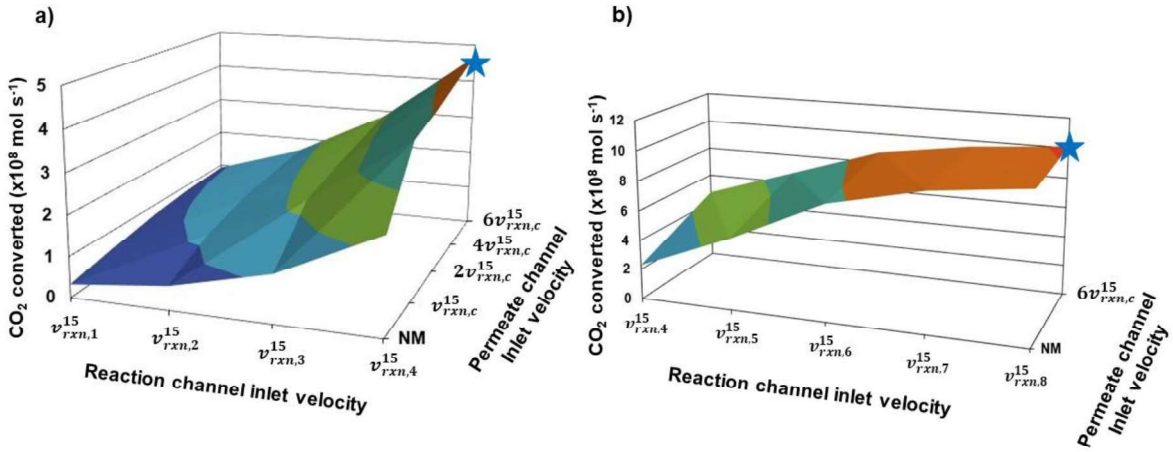

Figure 4.8. Effect of reaction and permeate channel inlet velocities on converted CO_2 amount at 15 bar (T = 523 K, H_2:CO_2 = 3, flow direction in membrane–integrated cases: co–current).

4.4. Effects of Reactor Pressure, Reaction and Permeate Channel Inlet Velocities and H_2:CO_2 Ratio on Syngas Composition

Syngas contains CO, CO_2 and H_2 gases and the composition of the multicomponent gas is one of the key points for many synthetic fuel production process. At 523 K, H_2:CO_2=3, permeate inlet velocity of $6v_{rxn,c}^{P}$ and $W/F_{CO_2} = 40$ g_{cat} h mol^{-1} for each operating pressure, the effect of reaction channel inlet velocity on syngas composition, defined in Equation 3.3, is investigated thoroughly. The ideal syngas composition is ~2, which the input for numerous syngas driven processes such as methanol and Fischer-Tropsch syntheses. The findings are presented in Figure 4.9.

As a general trend in this section, it is observed that syngas composition value is reduced with higher reaction channel inlet velocities. In contrast with 5 bar syngas composition results, 15 bar demonstrated higher syngas composition value. Thus, to achieve the targeted performance metric, 15 bar is studied comprehensively in terms of higher inlet velocities of reaction channel. At 5 bar, it is noted that the syngas composition is resulted much coherent to

the aimed syngas composition than 10 and 15 bar studies. The performance metric exhibited best performance at reaction channel velocity of $v_{rxn,4}^{5}$ in the range of this operating pressure. Furthermore, at 10 bar, it is observed that with the increasing pressure the syngas composition value is elevated. At lower reaction channel inlet velocities, it is also noticed that the performance metric is drifted away from the desired result. At the operating pressure of 10 bar and inlet velocity of $v_{rxn,4}^{10}$, the syngas composition is obtained as 3.3 which is an adequate result in the span of the operating pressure. In addition, the wide reaction channel inlet velocity range at 15 bar allows obtaining syngas composition near the desired value. At highest inlet velocity, $v_{rxn,8}^{15}$, syngas composition is achieved as 2.3. It is observed in these sets of simulations that, there is a trade-off between the more desired syngas composition values and CO_2 conversion due to requirement of higher inlet velocities and which causes less contact time between the catalyst and the feed stream.

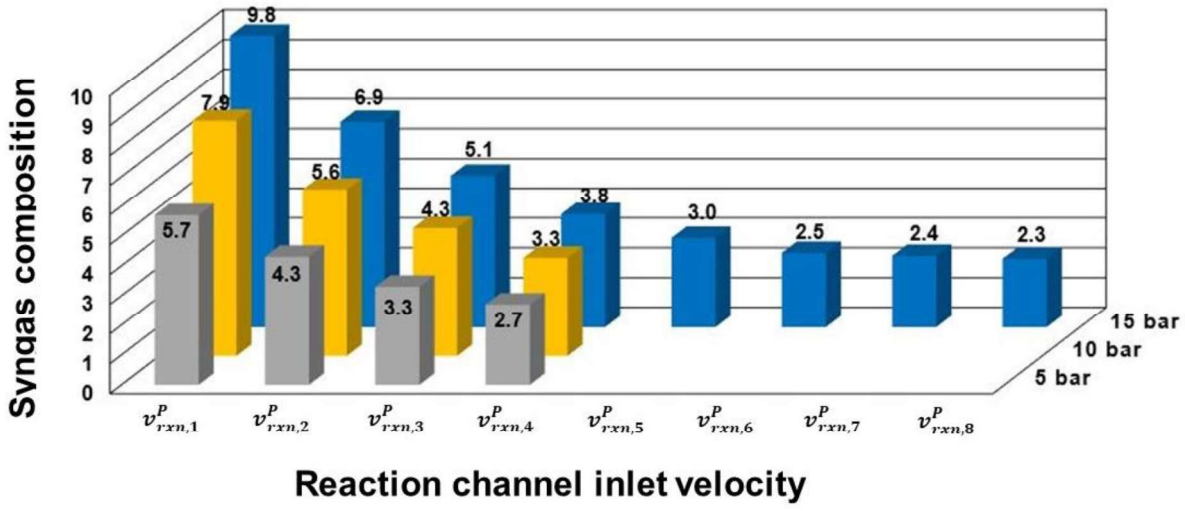

Figure 4.9. Effect of reaction channel inlet velocity and pressure on syngas composition (T = 523 K, H_2:CO_2 = 3, permeate channel inlet velocity: $6v_{rxn,c}^{p}$, flow direction in membrane–integrated cases: co–current).

At high inlet velocities, as it is mentioned before in Section 4.3. CO_2 conversion decreases to undesired levels. Therefore, an alternative way to optimize the syngas composition is to adjust the molar inlet H_2:CO_2 ratio Figure 4.10 Considering the significance of another performance metric, CO_2 conversion, the inlet velocities are selected which satisfies both considerable syngas composition values and CO_2 conversion. In this respect, inlet velocities of $v_{rxn,4}^{5}$ and $v_{rxn,4}^{15}$ are selected to be investigated. In addition, to examine the potential of achieving desired syngas composition value of 2, $v_{rxn,8}^{15}$ is also studied. At 5 bar, inlet velocity of $v_{rxn,4}^{5}$ and H_2:CO_2=2, it is observed that the syngas composition dropped below the desired value of 2, this indicates that between the H_2:CO_2 ratio of 2 and 4 there is an optimum point that produces syngas with a targeted composition. Increasing pressure to 15 bar at identical operating parameters resulted in unfavorable outcome. It is suggested for this case in order to reach the targeted value of the performance metric at the inlet velocity of $v_{rxn,4}^{15}$, H_2:CO_2=1 can be studied. At 15 bar, increasing the inlet velocity affected the syngas composition positively and value of 1.27 is achieved. This result also indicates that at 15 bar and $v_{rxn,8}^{15}$, syngas composition can be tuned accordingly.

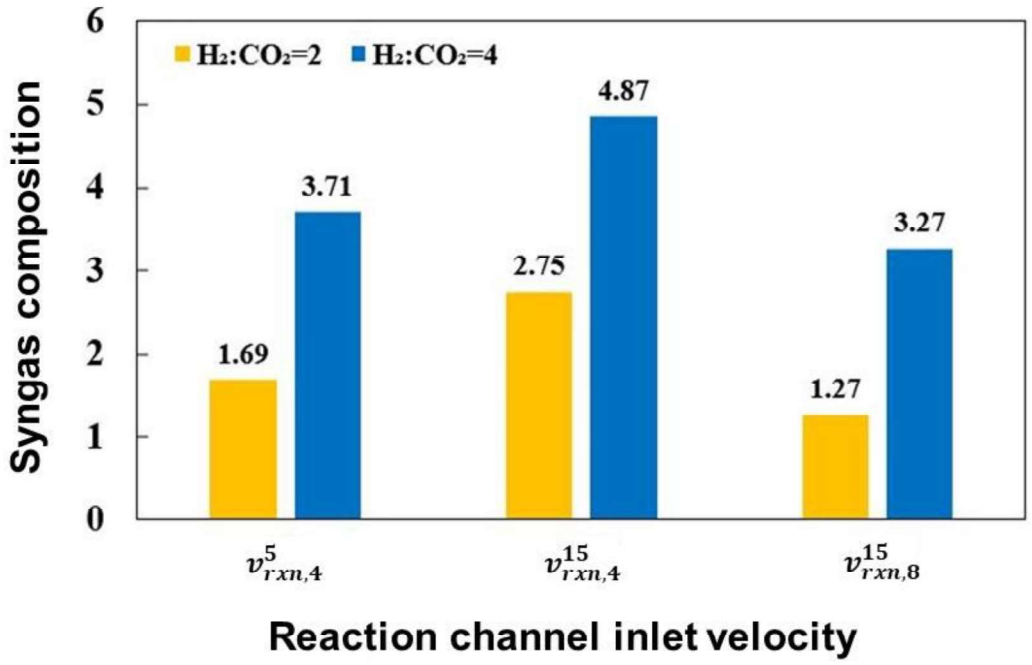

Figure 4.10. Effect of H_2:CO_2 ratio on syngas composition (T = 523 K, permeate channel inlet velocity: $6v_{rxn,c}^{p}$, flow direction in membrane–integrated cases: co–current).

4.5. Comparison of the Microchannel and Packed-Bed Membrane Reactors

The utilization of excess CO_2 in the atmosphere is one of the major concerns due to the global warming and climate change. In this respect, RWGS reaction gained importance in order to convert CO_2 into syngas with the assistance of H_2. To achieve this ecologically critical target, H_2 must be produced with green techniques. A commercial electrolyzer [68] which is energized by renewable energy is used in the context of the H_2 supply to the multichannel reactor. The electrolyzer has a H_2 production capacity of 18 kg h^{-1} which is equivalent to 2.5 mol s^{-1}. Thus, the production capacity of 2.5 mol H_2 s^{-1} is selected as basis capacity for the sizing of intensified multichannel reactor.

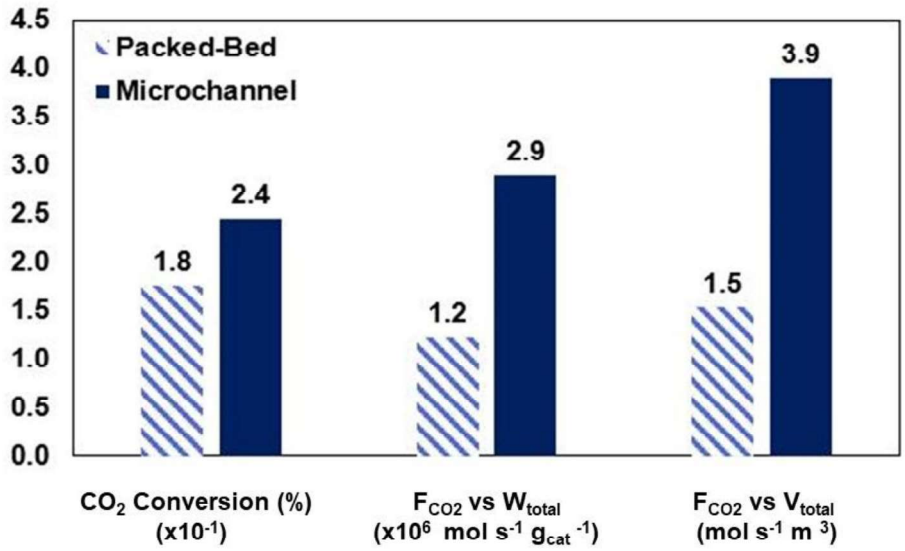

Figure 4.11. Comparison between multichannel and packed-bed reactors (T = 523 K, P = 5 bar, H_2:CO_2 = 3, permeate channel inlet velocity: $6v^{p}_{rxn,c}$, flow direction in membrane–integrated cases: co–current).

In order to assess the multichannel reactor, a comparison between the packed-bed membrane reactor which is investigated in the Section 3.2 is made [16]. It is observed that multichannel reactor is superior to the packed-bed reactor and it provides ~2.5 times higher CO_2 transformation per unit reactor volume and catalyst mass with ~33 % higher CO_2 conversion. Indicating that for both reactors transport limitations are negligible, the

performance difference between the reactors were as a result of greater membrane area per unit volume of the microchannel reactor. The flow paths in microreactor allows improved geometric approachability of the membrane which is closely correlated with the stronger (more than one order of magnitude higher) volumetric intensification [69]. Combining the benefits of great capability of scaling-up and producing syngas at the desired composition by tuning operating conditions indicates microchannel reactor is a more favorable route for syngas production via RWGS reaction, as can be seen in Figure 4.11.

4.6. Effect of Molar Inlet H_2:CO_2 Ratio on CO_2 conversion

The effect of H_2:CO_2 ratio on CO_2 conversion is investigated for varying pressures at 523 K, $W/F_{CO_2} = 40$ g_{cat} h mol^{-1}, permeate channel inlet velocity of $6v^{P}_{rxn,4}$, reaction channel inlet velocities of $v^{5}_{rxn,4}$ and $v^{15}_{rxn,4}$. In this respect, H_2:CO_2 ratios of 2-4 are studied and the results are presented in Figure 4.12.

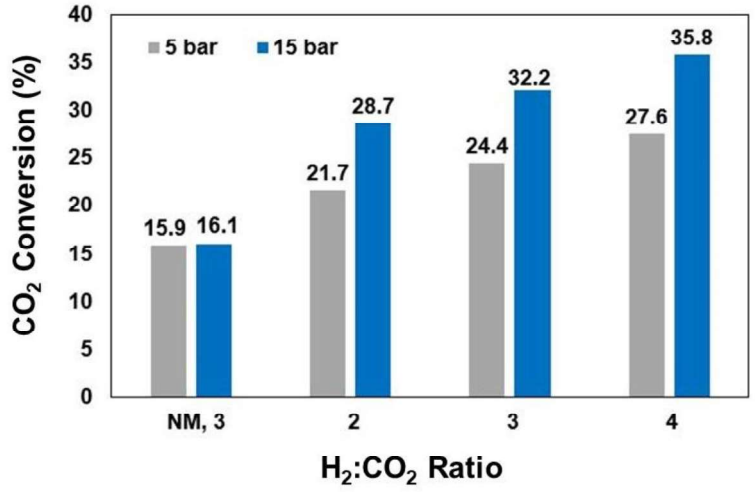

Figure 4.12. The effect of feed stream H_2:CO_2 ratio on CO_2 conversion at 5 and 15 bar (T = 523 K, permeate channel inlet velocity: $6v^{p}_{rxn,c}$, flow direction in membrane–integrated cases: co–current).

In order to observe the effect of the steam selective membrane and H_2:CO_2 ratio simultaneously on CO_2 conversion, case consist of feed stream H_2:CO_2 ratio of 3 in absence of the membrane is also studied. A monotonic rise is observed on CO_2 conversion with the increasing H_2:CO_2 ratio at both operating pressures of 5 and 15 bar. At H_2:CO_2=3 for 5 bar and 15 bar, CO_2 conversion is achieved as 24.4% and 32.2%, respectively with the integration of the hydrophilic membrane. In absence of the membrane, CO_2 conversion is suffered from the undesired product, steam, and conversion decreased to 15.9% and 16.1% respectively. Decreasing H_2:CO_2 ratio to 2, demonstrated a drop on the performance metric and conversion of 21.7 and 28.7 are achieved for each pressure. Thus, despite CO_2 is affected from H_2:CO_2 ratio, it is dominated by presence of the steam selective membrane. The conversion is decreased at H_2:CO_2=2, however it is still higher than the membraneless microreactor conversion at 5 bar. In addition, for each operating pressure, CO_2 conversion is maximized at H_2:CO_2=4. CO_2 conversion of 35.8% is obtained at 15 bar as the uppermost performance.

4.7. Impact of Permeate Channel Flow Configuration

In order to examine the combined effect of permeate channel flow configuration with pressure and H_2:CO_2 ratio, co- and counter-current flow configurations are investigated at 523 K, $W/F_{CO_2} = 40$ g_{cat} h mol^{-1}, reaction and permeate channel inlet velocities of $v^P_{rxn,4}$ and $6v^P_{rxn,4}$, respectively (Figure 4.13). It is observed CO_2 conversion simulated at 5 bar remained almost unchanged at the co- and counter-current configurations. For the case which is examined at H_2:CO_2 ratio of 2, the performance metric is evaluated as 21.7% and 21.6% respectively. In addition, for the ratio H_2:CO_2=4, CO_2 conversions for the both configurations turn out to be identical at 27.6%. Thus, at 5 bar the performance metric demonstrates almost identical results. The escalation in the operating pressure pursues the trend which is noted at 5 bar still in 15 bar results. CO_2 conversions at 15 bar and H_2:CO_2=2 are 28.7% and 30.3%, respectively, for both configurations. In addition, the increase in H_2:CO_2 ratio at the same pressure does not break the trend and with just about the equivalent margin, the results are obtained as 35.8% and 37.7%, respectively. At 15 bar, CO_2 conversions are found to be very close. It is concluded that flow configuration does not affect the reactor performance in the current range of operating conditions.

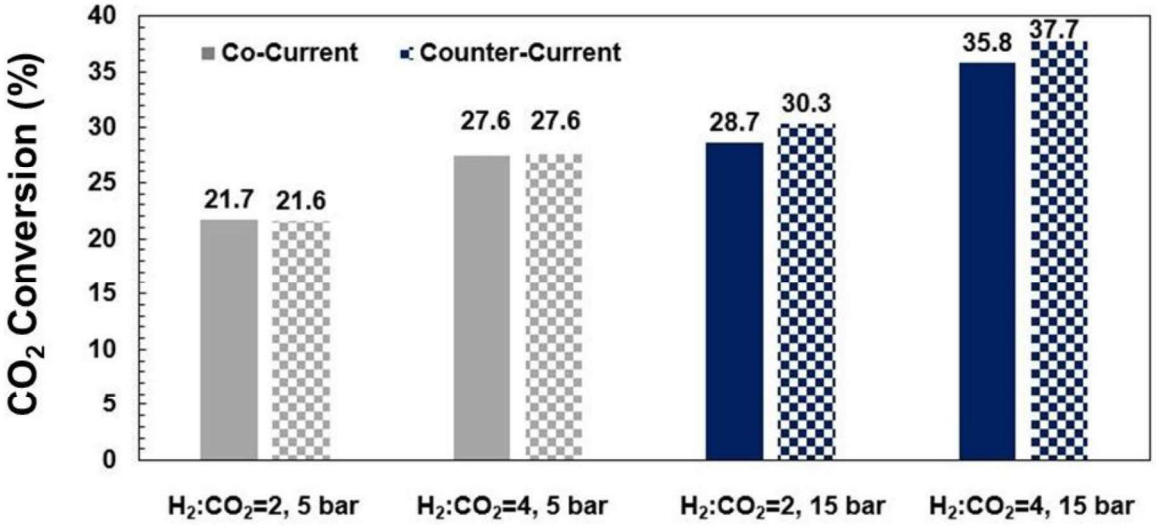

Figure 4.13. The effect of co- and counter-current permeate channel flows on CO_2 conversion at 5 and 15 bar (T = 523 K, permeate channel inlet velocity: $6v^{p}_{rxn,c}$).

5. CONCLUSION

Catalytic conversion of CO_2 and H_2 mixture to syngas via RWGS is modeled isothermally in a membrane separation integrated microchannel reactor. The reactor model is shown to capture the literature–based experimental data successfully. Due to the permselectivity of the SOD membrane to H_2O and H_2, the proposed intensified reactor is configured in a way to maximize CO_2 transformation by simultaneous transmembrane H_2 dosing into and H_2O removal from the reaction medium. The findings, all obtained at 523 K, show the effects of the operating conditions on per cent CO_2 conversion, the molar amount of CO_2 converted and syngas composition as summarized below:

5.1. Conclusions

- Fluid velocities at the reaction and permeate channel inlets affect reactor performance significantly. CO_2 conversion can be elevated at lower inlet velocities (i.e., longer residence time) of the H_2 + CO_2 mixture and higher inlet velocities of the sweep gas (H_2). These conditions favor the extent of cross–membrane H_2 supply that promotes RWGS kinetically and thermodynamically. The promotion is magnified by the ejection of product H2O into the permeate side.
- The maximum CO_2 conversion of 52 % is obtained at 15 bar, H_2:CO_2 = 3 at which the thermodynamic limit is 16.8 %. This superior performance is observed at minimized molar dosing of the H_2 + CO_2 mixture, which undesirably limits the amount of CO_2 converted and reduces the syngas production capacity of the multichannel reactor. Both performance metrics are positively correlated with reactor pressure and the inlet velocity (i.e., molar flow rate) of the sweep gas.
- Membrane integration introduces significant flexibility in molar composition of syngas which changes in the 2.3–9.8 range. The composition decreases by reducing reactor pressure and increasing the inlet velocity of the reactive mixture. Imposing the recommended value of ~2 (for high temperature FT synthesis, methanol and DME production) points out the most favorable set of operating conditions that can deliver syngas composition of 2.7 ($W/F_{CO_2,in}$ = 40 g_c h mol^{-1}; sweep gas inlet velocity = 6 × the pertinent reaction channel inlet velocity, 5 bar, H_2:CO_2 = 3).

Under these conditions, CO_2 conversion is 24.5 % which exceeds ~16 % of the membraneless case, and the amount of CO_2 converted is 3.5×10^{-8} mol s^{-1} which is ~53 % above 3.5×10^{-8} mol s^{-1} of the membraneless case.

- Syngas composition can be decreased further by reducing molar inlet H_2:CO_2 ratio. Despite a limited loss in CO_2 conversion, decreasing H_2:CO_2 from 3 to 2 allows syngas production in a composition range of 1.7 to 2.8 at 5 and 15 bar, respectively. The conclusions stated so far for the co–current flow of the reactive mixture and sweep streams remain almost unchanged when the dosing is carried out in the counter–current mode. Nevertheless, the negligible impact of flow partitioning is valid for the current set of operating conditions and is likely to change in favor of the counter–current flow at higher reactor pressures.
- Under equivalent operating conditions, the micro structured unit proposed herein can deliver ~2.5 times higher molar CO_2 consumption per mass of catalyst and reactor volume and ~33 % higher CO_2 conversion than a packed–bed membrane reactor.

5.2. Recommendations

The following studies are recommended for the improvement of the present work:

- Due to the importance of steam selective membrane to the intensification process of microchannel reactor, other hydrophilic membranes can be investigated regarding the H_2O permeability and H_2 perm-selectivity properties.
- Other catalysts for the reaction can be modeled in terms kinetic model for identical performance metrics and operating parameters then both results can be compared in order to improve the performance of the porous zone in the reaction channel.

REFERENCES

[1] Worldometer, "World Population by Year ", https://www.worldometers.info/world-population/world-population-by-year/, accessed on October 24, 2022.

[2] Zhu, M., Q. Ge, and X. Zhu, "Catalytic Reduction of CO_2 to CO via Reverse Water Gas Shift Reaction: Recent Advances in the Design of Active and Selective Supported Metal Catalysts", *Transactions of Tianjin University*, Vol. 26, No. 3, pp. 172–187, 2020.

[3] Ghasemian, S., A. Faridzad, P. Abbaszadeh, A. Taklif, A. Ghasemi, and R. Hafezi, "An Overview of Global Energy Scenarios by 2040: Identifying the Driving Forces Using Cross-Impact Analysis Method", *International Journal of Environmental Science and Technology*, Open Access, 2020.

[4] Daza, Y. A. and J. N. Kuhn, "CO_2 Conversion by Reverse Water Gas Shift Catalysis: Comparison of Catalysts, Mechanisms and Their Consequences for CO_2 Conversion to Liquid Fuels", *RSC Advances*, Vol. 6, No. 55, pp. 49675–49691, 2016.

[5] Najari, S., G. Gróf, and S. Saeidi, "Enhancement of Hydrogenation of CO_2 to Hydrocarbons via In-Situ Water Removal", *International Journel of Hydrogen Energy*, Vol. 44, No. 45, pp. 24759–24781, 2019.

[6] González-Castaño, M., J. González-Arias, M. E. Sánchez, J. Cara-Jiménez, and H. Arellano-García, "Syngas Production Using CO_2-Rich Residues: From Ideal to Real Operating Conditions", *Journal of CO_2 Utilization*, Vol. 52, pp. 101661–101670, 2021.

[7] Yang, X. X. Su, X. Chen, H. Duan, B. Liang, Q. Liu, X. Liu, Y. Ren, Y. Huang and T. Zhang, "Promotion Effects of Potassium on the Activity and Selectivity of Pt/Zeolite Catalysts for Reverse Water Gas Shift Reaction", *Applied Catalysis B*, Vol. 216, pp. 95–105, 2017.

[8] Najari, S., G. Gróf, and S. Saeidi, "Enhancement of Hydrogenation of CO_2 to Hydrocarbons via In-Situ Water Removal", *International Journel of Hydrogen Energy*, Vol. 44, No. 45, pp. 24759–24781, 2019.

[9] González-Castaño, M., B. Dorneanu, and H. Arellano-García, "The Reverse Water-Gas Shift Reaction: A Process Systems Engineering Perspective", *Reaction Chemistry and Engineering*, Vol. 6, No. 6, pp. 954–976, 2021.

[10] Zhou, G., F. Xie, L. Deng, G. Zhang, and H. Xie, "Supported Mesoporous $Cu/CeO_{2-\delta}$ Catalyst for CO_2 Reverse Water–Gas Shift Reaction to Syngas", *International Journel of Hydrogen Energy*, Vol. 45, No. 19, pp. 11380–11393, 2020.

[11] Daza, Y. A., and J. N. Kuhn, "CO_2 Conversion by Reverse Water-Gas Shift Catalysis: Comparison of Catalysts, Mechanisms and Their Consequences for CO_2 Conversion to Liquid Fuels", *RSC Advances*, Vol. 6, No. 55, pp. 49675–49691, 2016.

[12] Rezaei E., and S. Dzuryk, "Techno-Economic Comparison of Reverse Water-Gas Shift Reaction to Steam and Dry Methane Reforming Reactions for Syngas Production", *Chemical Engineering Research and Design*, Vol. 144, pp. 354–369, 2019.

[13] Van Kampen, J., J. Boon, F. van Berkel, J. Vente, and M. van Sint Annaland, "Steam Separation Enhanced Reactions: Review and outlook", *Chemical Engineering Journal*, Vol. 374, pp. 1286–1303, 2019.

[14] Li, Z., Y. Deng, N. Dewangan, J. Hu, Z. Wang, X. Tan, S. Liu and S. Kawi, "High Temperature Water Permeable Membrane Reactors for CO_2 Utilization", *Chemical Engineering Journal*, Vol. 420, pp. 129834–129835, 2021.

[15] Venvik, H. J., and J. Yang, "Catalysis in Microstructured Reactors: Short Review on Small-Scale Syngas Production and Further Conversion into Methanol, DME and Fischer-Tropsch Products", *Catalysis Today*, Vol. 285, pp. 135–146, 2017.

[16] Dzuryk S. and E. Rezaei, "Intensification of the Reverse Water Gas Shift Reaction by Water-Permeable Packed-Bed Membrane Reactors", *Industrial & Engineering Chemistry Research*, Vol. 59, No. 42, pp. 18907–18920, 2020.

[17] Wang, S., H. Liu, Y. Chen, and S. Yang, "Reverse Water–Gas Shift Reaction over Co-Precipitated Co–CeO_2 Catalysts: Effect of Co Content on Selectivity and Carbon Formation", *International Journel of Hydrogen Energy*, Vol. 42, No. 6, pp. 3682–3689, 2017.

[18] Zhang, L., L. Chen, S. Xia, C. Wang, and F. Sun, “Entropy Generation Minimization for Reverse Water Gas Shift (RWGS) Reactors”, *Entropy*, Vol. 20, No. 6, pp. 415–437, 2018.

[19] Zhao, Z., M. Wang, P. Ma, Y. Zheng, J. Chen, H. Li, X. Zhang, K. Zheng, Q. Kuang and Z. X. Xie, “Atomically Dispersed Pt/CeO_2 Catalyst with Superior CO Selectivity in Reverse Water-Gas Shift Reaction”, *Applied Catalysis B*, Vol. 291, pp. 120101–120109, 2021.

[20] Chen, X., X. Su, H. Duan, B. Liang, Y. Huang, and T. Zhang, “Catalytic Performance of the Pt/Tio_2 Catalysts in Reverse Water Gas Shift Reaction: Controlled Product Selectivity and a Mechanism Study”, *Catalysis Today*, Vol. 281, pp. 312–318, 2017.

[21] Bobadilla, L. F., J. L. Santos, S. Ivanova, J. A. Odriozola, and A. Urakawa, “Unravelling the Role of Oxygen Vacancies in the Mechanism of the Reverse Water-Gas Shift Reaction by Operando DRIFTS and Ultraviolet-Visible Spectroscopy”, *ACS Catalysis*, Vol. 8, No. 8, pp. 7455–7467, 2018.

[22] Nelson, N. C., L. Chen, D. Meira, L. Kovarik, and J. Szanyi, “In-Situ Dispersion of Palladium on TiO_2 During Reverse Water–Gas Shift Reaction: Formation of Atomically Dispersed Palladium”, *Angewandte Chemie - International Edition*, Vol. 59, No. 40, pp. 17657–17663, 2020.

[23] Jin, R., J. Easa, and C. P. O’Brien, “Highly Active CuO_x/SiO_2Dot Core/Rod Shell Catalysts with Enhanced Stability for the Reverse Water Gas Shift Reaction”, *ACS Appl Materials & Interfaces*, Vol. 13, No. 32, pp. 38213–38220, 2021.

[24] Zhang, Y. L. Liang, Z. Chen, J. Wen, W. Zhong, S. Zou, M. Fu, L. Chen and D. Ye, “Highly Efficient Cu/CeO_2-Hollow Nanospheres Catalyst for the Reverse Water-Gas Shift Reaction: Investigation on the Role of Oxygen Vacancies Through In-Situ UV-Raman and DRIFTS”, *Appl Surface Science*, Vol. 516, pp. 146035–146045, 2020.

[25] Chen, L., D. Wu, C. Wang, M. Ji, and Z. Wu, “Study on $Cu\text{-}Fe/CeO_2$ Bimetallic Catalyst for Reverse Water-Gas Shift Reaction”, *Journal of Environmental Chemical Engineering*, Vol. 9, No. 3, pp. 105183–105189, 2021.

[26] Bahmanpour, A. M., F. Héroguel, M. Kilic, C. J. Baranowski, L. Artiglia, U. Röthlisberger, J. S. Luterbacher and O. Krocher, “Cu-Al Spinel as a Highly Active

and Stable Catalyst for the Reverse Water Gas Shift Reaction", *ACS Catalysis*, Vol. 9, No. 7, pp. 6243–6251, 2019.

[27] Jurković, D. L., A. Pohar, V. D. B. C. Dasireddy, and B. Likozar, "Effect of Copper-based Catalyst Support on Reverse Water-Gas Shift Reaction (RWGS) Activity for CO_2 Reduction", *Chemical Engineering & Technologies*, Vol. 40, No. 5, pp. 973–980, 2017.

[28] Liu H. X., S. Q. Li, W. W. Wang, W. Z. Yu, W. J. Zhang, C. Ma and C. J. Mia, "Partially Sintered Copper–Ceria as Excellent Catalyst for the High-Temperature Reverse Water-Gas Shift Reaction", *Nature Communications*, Vol. 13, No. 1, pp. 867–877, 2022.

[29] Pastor-Pérez, L., F. Baibars, E. le Sache, H. Arellano-García, S. Gu, and T. R. Reina, "CO_2 Valorisation via Reverse Water-Gas Shift Reaction Using Advanced Cs Doped Fe-Cu/Al_2O_3 Catalysts", *Journal of CO_2 Utilization*, Vol. 21, pp. 423–428, 2017.

[30] Ronda-Lloret, M., S. Rico-Francés, A. Sepúlveda-Escribano, and E. v. Ramos-Fernandez, "CuO_x/CeO_2 Catalyst Derived from Metal Organic Framework for Reverse Water-Gas Shift Reaction", *Applied Catalysis A Gen*, Vol. 562, pp. 28–36, 2018.

[31] He, Y. K. R. Yang, Z. Yu, Z. S. Fishman, L. A. Achola, Z. M. Tobin, J. A. Heinlein, S. Hu, S. L. Suib, V. S. Batista and L. D. Pfefferle, "Catalytic Manganese Oxide Nanostructures for the Reverse Water Gas Shift Reaction", *Nanoscale*, Vol. 11, No. 35, pp. 16677–16688, 2019.

[32] Yang, L., L. Pastor-Pérez, S. Gu, A. Sepúlveda-Escribano, and T. R. Reina, "Highly Efficient Ni/CeO_2-Al_2O_3 Catalysts for CO_2 Upgrading via Reverse Water-Gas Shift: Effect of Selected Transition Metal Promoters", *Applied Catalysis B*, Vol. 232, pp. 464–471, 2018.

[33] Peng, L., B. Jurca, A. Primo, A. Gordillo, V. I. Parvulescu, and H. García, "Co-Fe Clusters Supported on N-Doped Graphitic Carbon as Highly Selective Catalysts for Reverse Water Gas Shift Reaction", *ACS Sustainable Chemistry & Engineering*, Vol. 9, No. 28, pp. 9264–9272, 2021.

[34] Ma, Y., Z. Guo, Q. Jiang, K. H. Wu, H. Gong, and Y. Liu, "Molybdenum Carbide Clusters for Thermal Conversion of CO_2 to CO via Reverse Water-Gas Shift Reaction", *Journal of Energy Chemistry*, Vol. 50, pp. 37–43, 2020.

[35] Morse, J. R., M. Juneau, J. W. Baldwin, M. D. Porosoff, and H. D. Willauer, "Alkali Promoted Tungsten Carbide as a Selective Catalyst for the Reverse Water Gas Shift Reaction", *Journal of CO_2 Utilization*, Vol. 35, pp. 38–46, 2020.

[36] Kim, S. S., H. H. Lee, and S. C. Hong, "A Study on the Effect of Support's Reducibility on the Reverse Water-Gas Shift Reaction over Pt Catalysts", *Applied Catalysis A*, Vol. 423–424, pp. 100–107, 2012.

[37] Wolf, A., A. Jess, and C. Kern, "Syngas Production via Reverse Water-Gas Shift Reaction over a Ni-Al_2O_3 Catalyst: Catalyst Stability, Reaction Kinetics, and Modeling", *Chemical Engineering & Technology*, Vol. 39, No. 6, pp. 1040–1048, 2016.

[38] Munera Parra, A. A., C. Asmanoglo, and D. W. Agar, "Modelling and Optimization of a Moving-Bed Adsorptive Reactor for the Reverse Water-Gas Shift Reaction", *Computers & Chemical Engineering*, Vol. 109, pp. 203–215, 2018.

[39] Pieterse, J. A. Z., G. D. Elzinga, S. Booneveld, J. van Kampen, and J. Boon, "Reactive Water Sorbents for the Sorption-Enhanced Reverse Water–Gas Shift", *Catalysis Letters*, Vol. 152, No. 2, pp. 460–466, 2022.

[40] Ghodhbene, M., F. Bougie, P. Fongarland, and M. C. Iliuta, "Hydrophilic Zeolite Sorbents for In-situ Water Removal in High Temperature Processes", *Canadian Journal of Chemical Engineering*, Vol. 95, No. 10, pp. 1842–1849, 2017.

[41] Lee, J., H. G. Park, M. H. Hyeon, B. G. Kim, S. K. Kim, and S. Y. Moon, "Low-Temperature CO_2 Hydrogenation Overcoming Equilibrium Limitations with Polyimide Hollow Fiber Membrane Reactor", *Chemical Engineering Journal*, Vol. 403, pp. 126457–126466, 2021.

[42] Lafleur, M., F. Bougie, N. Guilhaume, F. Larachi, P. Fongarland, and M. C. Iliuta, "Development of a Water-Selective Zeolite Composite Membrane by a New Pore-Plugging Technique", *Microporous and Mesoporous Materials*, Vol. 237, pp. 49–59, 2017.

[43] Sohn S. and S. H. Yoon, “Numerical Study of Heat and Mass Transfer by Reverse Water-Gas Shift Reaction in Catalyst-Coated Microchannel Reactor”, *Journal of Mechanical Science and Technology*, Vol. 34, No. 5, pp. 2207–2216, 2020.

[44] Engelbrecht, N., S. Chiuta, R. C. Everson, H. W. J. P. Neomagus, and D. G. Bessarabov, “Experimentation and CFD Modelling of a Microchannel Reactor for Carbon Dioxide Methanation”, *Chemical Engineering Journal*, Vol. 313, pp. 847–857, 2017.

[45] Koybasi, H.H. and A. K. Avci, “Modeling of a Membrane Integrated Catalytic Microreactor for Efficient DME Production from Syngas with CO_2”, *Catalysis Today*, Vol. 383, pp. 133–145, 2022.

[46] Koybasi, H.H., C. Hatipoglu, and A. K. Avci, “Sustainable DME Synthesis from CO_2–Rich Syngas in a Membrane Assisted Reactor–Microchannel Heat Exchanger System”, *Journal of CO_2 Utilization*, Vol. 52, pp. 101660–101668 , 2021.

[47] Wang, N., Y. Liu, A. Huang, and J. Caro, “Supported SOD Membrane with Steam Selectivity by a Two-Step Repeated Hydrothermal Synthesis”, *Microporous and Mesoporous Materials*, Vol. 192, pp. 8–13, 2014.

[48] Raso, R. M. Tovar, J. Lasobras, J. Herguido, I. Kumakiri, S. Araki and M. Menendez “Zeolite Membranes: Comparison in the Separation of $H_2O/H_2/CO_2$ Mixtures and Test of a Reactor for CO_2 Hydrogenation to Methanol”, *Catalysis Today*, Vol. 364, pp. 270–275, 2021.

[49] Wilson, M. E., N. Kota, Y. T. Kim, Y. Wang, D. B. Stolz, P. R. LeDuc and O. B. Ozdoganlar, “Fabrication of Circular Microfluidic Channels by Combining Mechanical Micromilling and Soft Lithography”, *Lab on a Chip*, Vol. 11, No. 8, pp. 1550–1555, 2011.

[50] Uriz, I., G. Arzamendi, E. López, J. Llorca, and L. M. Gandía, “Computational Fluid Dynamics Simulation of Ethanol Steam Reforming in Catalytic Wall Microchannels”, *Chemical Engineering Journal*, Vol. 167, No. 2–3, pp. 603–609, 2011.

[51] Peláez, R., P. Marín, and S. Ordóñez, “Direct Synthesis of Dimethyl Ether from Syngas Over Mechanical Mixtures of $CuO/ZnO/Al_2O_3$ and Γ-Al_2O_3: Process Optimization and Kinetic Modelling”, *Fuel Processing Technology*, Vol. 168, pp. 40–49, 2017.

[52] Koybasi, H. H. and A. K. Avci, "Numerical Analysis of CO_2-to-DME Conversion in a Membrane Microchannel Reactor", *Industrial & Engineering Chemistry Research*, Vol. 61, No. 30, pp. 10846–10859, 2022.

[53] Pastor-Pérez, L., M. Shah, E. le Saché, and T. R. Reina, "Improving Fe/Al_2O_3 Catalysts for the Reverse Water-Gas Shift Reaction: On the Effect of Cs as Activity/Selectivity Promoter", *Catalysts*, Vol. 8, No. 12, pp. 608–621, 2018.

[54] Tozar, U. and A. K. Avci, "Strategies for Improving CO_2 Utilization in Microchannel Enabled Production of Dimethyl Ether", *Chemical Engineering and Processing - Process Intensification*, Vol. 151, pp. 107914–107925, 2020.

[55] Ozturk, N. F. and A. K. Avci, "Intensified Dimethyl Ether Production from Synthesis Gas with CO_2", *Chemical Engineering Journal*, Vol. 370, pp. 885–896, 2019.

[56] Ehrfeld, W., V. Hessel, H. Lowe, "Microreactors - New Technology for Modern Chemistry", *Organic Process Research & Development*, Vol. 5, No. 1, pp. 89–89, 2001.

[57] Veser G., and J. Frauhammer, "Modelling Steady State and Ignition During Catalytic Methane Oxidation in a Monolith Reactor", *Chemical Engineering Science*, Vol. 55, No. 12, 2000.

[58] Sun, J. T., I. S. Metcalfe, and M. Sahibzada, "Deactivation of Cu/ZnO/Al_2O_3 Methanol Synthesis Catalyst by Sintering", *Industrial & Engineering Chemistry Research*, Vol. 38, No. 10, pp. 3868–3872, 1999.

[59] Mcbride, B. J., S. Gordon, A. Cleveland, and M. A. Reno, "NASA Technical Memorandum 4513 Coefficients for Calculating Thermodynamic and Transport Properties of Individual Species", https://ntrs.nasa.gov/search.jsp? R=19940013151, accessed on December 2, 2022.

[60] Ginés, M. J. L., A. J. Marchi, and C. R. Apesteguía, "Kinetic Study of the Reverse Water-Gas Shift Reaction over CuO/ZnO/Al_2O_3 Catalysts", *Applied Catalysis A General*, Vol. 154, No. 1–2, pp. 155–171, 1997.

[61] Ji,G., G. Wang, K. Hooman, S. Bhatia, and J. C. Diniz da Costa, "Computational Fluid Dynamics Applied to High Temperature Hydrogen Separation Membranes", *Frontiers of Chemical Science and Engineering*, Vol. 6, No. 1. pp. 3–12, 2012.

[62] Wang, N., Y. Liu, A. Huang, and J. Caro, "Hydrophilic SOD and LTA Membranes for Membrane-Supported Methanol, Dimethylether and Dimethylcarbonate Synthesis", *Microporous and Mesoporous Materials*, Vol. 207, pp. 33–38, 2015.

[63] Tan, X., and K. Li, "Membrane Microreactors for Catalytic Reactions", *Journal of Chemical Technology and Biotechnology*, Vol. 88, No. 10. pp. 1771–1779, 2013.

[64] Farjoo, A., S. M. Kuznicki, and M. Sadrzadeh, "Hydrogen Separation by Natural Zeolite Composite Membranes: Single and Multicomponent Gas Transport", *Materials*, Vol. 10, No. 10, pp. 1159–1172, 2017.

[65] Bac, B. and A. K. Avci, "Ethylene Oxide Synthesis in a Wall-Coated Microchannel Reactor with Integrated Cooling", *Chemical Engineering Journal*, Vol. 377, pp. 120104–120113, 2019.

[66] Tezcan, I. and A. K. Avci, "Parametric Investigation of Oxidative Coupling of Methane in a Heat-Exchange Integrated Microchannel Reactor", *Journal of Chemical Technology and Biotechnology*, Vol. 90, No. 10, pp. 1827–1838, 2015.

[67] Delparish, A. and A. K. Avci, "Modeling of Intensified Glycerol Steam Reforming in a Heat-Exchange Integrated Microchannel Reactor," *Catalysis Today*, Vol. 299, pp. 328–338, 2018.

[68] Plugpower, "The 1MW Electrolyzer." , 2020, https://www.plugpower.com/wp-content/uploads/2020/10/2020_1MWELX_Spec021721_F.pdf, accessed on November 30, 2022.

[69] Kolb, G. "Review: Microstructured Reactors for Distributed and Renewable Production of Fuels and Electrical Energy", *Chemical Engineering and Processing: Process Intensification*, Vol. 65. pp. 1–44, 2013.

APPENDIX A: PACKED-BED MEMBRANE REACTOR MODEL EQUATIONS

1-D modeling of a packed-bed membrane reactor is adopted from the study of Dzuryk and Rezaei [16]. In this regard, a reactor tube with length and radius of 5 and 5×10^{-3} m, respectively, is considered. Using the tubular reactor volume of 3.93×10^{-4} m^3 and catalyst bed density of 2657 kg m^{-3} [16], the mass of catalyst packed into PBMR is computed as 1.043 kg. Using the comparison basis of T=523 K, P= 5 bar, W/F_{CO_2} = 40 g_c h mol^{-1} and molar inlet H_2:CO_2 ratio of 3, inlet molar flow rates of H_2 ($F_{H_2,in}$) and CO_2 ($F_{CO_2,in}$) are determined and used as the initial values to the isothermal, steady–state, one–dimensional pseudohomogeneous packed bed reactor model. The model is represented by

$$\frac{dF_i}{dW} = R_i - Perm_i\left(p^i_{rxn} - p^i_{perm}\right) \qquad i = H_2O, H_2\,, \tag{A.1}$$

$$\frac{dF_i}{dW} = R_i \qquad i = CO, CO_2\,, \tag{A.2}$$

$$R_{\mathrm{CO}} = r,\ R_{\mathrm{H_2O}} = r;\ R_{\mathrm{CO_2}} = -r;\ R_{\mathrm{H_2}} = -r; r = r_{RWGS}\,, \tag{A.3}$$

$$\text{At } W = 0;\ F_{CO_2} = F_{CO_2,in};\ F_{H_2} = F_{H_2,in};\ F_{CO} = F_{H_2O} = 0. \tag{A.4}$$

In this model, partial pressure of H_2 in the permeate channel is assumed to remain unchanged. Additionally, $p^{H_2O}_{perm}$ is taken ~0 (amount of H_2O in the sweep gas is neglected). For direct comparison with the microchannel reactor operating without any diffusion limitations (see Section 2), the PBMR model assumes the presence of a "pseudohomogeneous" phase in the reactor in which mass–based diffusion resistances are disregarded. The resulting set of ordinary differential equations is solved numerically by using the *ode15* solver in MATLAB (v. R2021a). The span of numerical integration is taken between 0 and 1.043 kg, the catalyst amount computed above. Permeability values for H_2 and H_2O specific for the SOD membrane material are given in Section 3.3. Using its simulated exit molar flow rate, CO_2 conversion and amount of CO_2 converted (Equation 3.1 and Equation 3.2, respectively) are calculated.